Evaluation of GPM IMERG Product Over the Yellow River Basin Using an Improved Error-Component Procedure

Yunfei Tian , *Student Member, IEEE*, Xiaoyu Lv , Hao Guo , Junli Li , Xiangchen Meng , *Member, IEEE*, Chunrui Guo , Li Zhu , and Philippe De Maeyer , *Member, IEEE*

Abstract—In the global precipitation measurement (GPM) era, the integrated multisatellite retrievals for GPM (IMERG) stands as a pivotal precipitation algorithm. This study aims to evaluate the accuracy of IMERG in capturing precipitation frequency and volume in the Yellow River Basin, China. Four satellite-based precipitation estimates (SPEs) from three algorithmic versions of IMERG were analyzed on an hourly scale using gauge observations. An improved error component procedure was employed to identify error sources. Results showed that all four IMERG products effectively captured the spatial distribution patterns and seasonal changes of precipitation, IMERG_F demonstrated the best overall performance, followed by IMERG_L, while IMERG_E performed the worst. However, they tended to overestimate precipitation. IMERG_F_Cal performed the best for precipitation frequency detection, with the highest probability of detection (POD $= 52.7\%$) and the lowest missed events (MIS $= 47.3\%$). Error component analysis highlights false bias as the main source of error, followed by missed bias. In winter, missed bias was the primary error source. Notably, a significant overestimation of precipitation was observed along the Yellow River. In detail, false bias dominated IMERG_E, IMERG_L, and IMERG_F_UnCal below 800 m in spring, summer, and autumn. However, in winter, missed bias became the primary error source for these three products at elevations above 200m and for IMERG_F_Cal above 500 m. IMERG_F_Cal exhibited false bias as the primary error source in all seasons. Suggested algorithm developers focus on improving IMERG SPEs' identification capabilities for light precipitation events and rainstorms. Findings can provide a reference for improving the IMERG product algorithms and enhancing users' understanding of the error characteristics and sources of IMERG products.

I. Introduction

PRECIPITATION is a crucial component of the Earth's water cycle, with significant implications for the atmosphere, hydrosphere, and biosphere [1], [2], [3]. Accurate and timely information about the distribution of precipitation in terms of space and time is essential for various applications, such as water resource assessment and management, flood warnings, and the study of extreme precipitation events. Satellite remote sensing technology, along with onboard sensing equipment, has rapidly advanced and improved, enabling the development of multisatellite precipitation products. These products address the limitations and drawbacks of ground-based rain gauges and radar systems and have become the primary technology for obtaining high-resolution precipitation information at both spatial and temporal scales [4]. Integrated Multi-Satellite Retrievals for GPM (IMERG) represents the latest generation of multisatellite integrated precipitation data designed for the Global Precipitation Measurement (GPM) mission [5]. The IMERG data production system consists of three processing stages. In the real-time phase, the system runs the forward propagation algorithm, known as the cloud-moving vector propagation algorithm, to generate early data (IMERG_E). Subsequently, the system runs again, incorporating the backward propagation algorithm to generate late data (IMERG_L). Finally, the system performs another run to produce final data (IMERG_F) by including the monthly scale surface precipitation data for correction [6]. These three processing stages cater to the diverse needs of different data users. However, the accuracy of the inversion process in IMERG has been a subject of interest for numerous researchers [3], [7], [8], [9].

In recent years, numerous scholars have conducted preliminary evaluations of the error characteristics of IMERG. Research findings have demonstrated the strong performance of IMERG across various time scales [1], [10], [11], [12]. Based on extensive comparisons, the previous studies proved that it is important to acknowledge that the sources of precipitation retrieval errors are complex and diverse. The accuracy of precipitation retrieval is influenced by various factors, including sensors, algorithms,

geographical features, climatic conditions, and precipitation characteristics. For example, Bulovic et al. [13] found that the choice of sensor sources or algorithms is an important error source in satellite-based precipitation retrieval [3], [6]. A study conducted by Kim et al. [14] found that the IMERG Final product and the tropical rainfall measuring mission (TRMM) 3B42V7 exhibited high uncertainties from the orographic convection and land–ocean classification algorithm. In addition, the presence of complex terrain and intricate precipitation patterns can introduce significant uncertainties for satellite data evaluation [15].

The GPM core observatory satellite is equipped with the dual-frequency phased array precipitation radar and the multichannel GPM microwave imager, which offers potentially enhanced capabilities for estimating light precipitation and snow [16]. There has been a particular focus on the evaluation of IMERG's capability in retrieving light rainfall among researchers. It is found that IMERG exhibits inconsistent performance in detecting light precipitation [1], [9], [13]. For example, Tang et al. [1] found GPM has satisfactory performance in capturing light precipitation events over Mainland China, while Chen et al. [9] proved IMERG has limited capability in estimating light precipitation. Furthermore, passive microwave (PMW) sensors were proven to have deficiencies in distinguishing precipitation from a frozen/snow surface [6], [17], [18], [19].

The aforementioned research findings provide valuable insights for both IMERG algorithm developers and data users. Most studies commonly employ traditional evaluation methods that entail comparing satellite-derived precipitation data with ground-based observations, or furtherly including environmental factors, such as terrain characteristics and precipitation intensity. Typically, these evaluation methods compute the total bias using satellite precipitation estimates (SPEs) minus ground observations, which ignore the interdependence among various indicators [20].

To address these limitations, Tian et al. [21] proposed the error component method, which helps identify the sources of error in satellite precipitation data. The process of precipitation estimation usually consists of two steps [21], [22]. The first step is screening, which involves distinguishing rainfall pixels from nonrainfall pixels. This step can introduce two types of errors. Failure to detect rainfall pixels leads to missed precipitation (i.e., missed bias), while nonrainfall pixels may be incorrectly classified as rainfall pixels, resulting in false precipitation (i.e., false bias). Once the rainfall pixels are identified, the second step is to establish the relationship between the observed bright temperature data (from PMW or IR) and rainfall rate. Even in cases where rainfall pixels are correctly detected, the conversion of bright temperature data to rainfall rates is subject to error (i.e., hit bias). By considering these error components, the error component method provides a more comprehensive analysis of the sources of errors in satellite precipitation data and helps algorithm developers and data users gain a deeper understanding of the error characteristics of satellite precipitation and its generation mechanisms [20]. In the satellite inversion process of precipitation, two types of errors are involved: event occurrence errors and precipitation errors [23]. Event occurrence errors can be evaluated using metrics, such as the correct detection rate

(POD), false alarm rate (FAR), and missing alarm rate (MIS). On the other hand, the error component method decomposes the total bias into three independent components: hit bias, false bias, and missed bias. Based on the error-component method, Tang et al. [24] furtherly decomposed the hit bias into both systematic and random errors by using a multiplicative model. Systematic errors arise from the characteristics of the remote sensing measurement or inversion algorithms, and random errors arise from the sensor sampling and design [1], [24]. This approach allows for a more accurate quantification of uncertainty. In recent years, the temporal scale of verification has advanced from monthly and daily scales [25], [26] to an hourly scale [9], [18], [27], [28]. Li et al. [19], [29] analyzed the characteristics of IMERG from the perspective of precipitation events and tracked its ability to capture the evolution of errors throughout the precipitation process. Chen et al. [9] conducted a comparative analysis of six purely satellite-derived global precipitation datasets and found that the false bias is the dominant error source for these products in the cold season over semi-humid areas. Furthermore, studies have indicated that over the coastal regions, IMERG tends to overestimate heavy precipitation by approximately 25% [18]. These research findings provide guidance for applications of IMERG. However, the aforementioned studies predominantly focus on the evaluation of IMERG Final as a representative compared to other products, or solely evaluated different IMERG versions using traditional total-bias-based methods. There is a limited amount of research tracing the error sources among the three different types of IMERG (early, late, and final run) and the comparison between corrected and uncorrected versions (Cal and Uncal), particularly in China.

The Yellow River Basin in China is a crucial ecological region that faces significant ecological and environmental challenges. Among these challenges, water resource scarcity is one of the most pressing issues, and there are considerable variations in water resource distribution among the upstream, midstream, and downstream areas. In addition, the Yellow River Basin holds vital importance as a key ecological functional area in China. SPEs served as essential data sources for meteorological monitoring, hydrological modeling, ecological assessment, and more. However, errors in SPEs can impact the accuracy of various applications. Therefore, conducting studies on the error characteristics of SPEs in the Yellow River Basin holds great significance for these applications in the Yellow River Basin [15], [30], [31].

Taking the Yellow River basin as the study area, this study focuses on the trace of the error sources of IMERG products by comparing estimates from different versions (early, late, and final with and without error correction) and using the improved error component analysis. In addition, the dependence of error components on both precipitation intensity and elevation was also included in this study. Specifically, the objectives include the following.

1) To compare the error characteristics between IMERG SPEs at an hourly scale from both precipitation amount and frequency error perspectives.
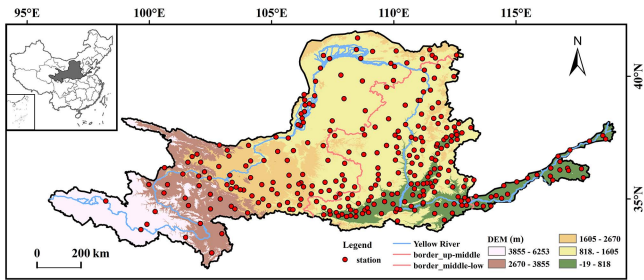2) To track the sources of errors based on an improved error component method.

Fig. 1. Terrain and spatial distribution of the meteorological stations in the Yellow River Basin.

3) To investigate the influence of elevation and precipitation intensity on the error components in IMERG SPEs.

The findings of this study could serve as valuable scientific references for data users in data selection, potential error propagation estimation when used in various applications and water resources management in the Yellow River Basin. In addition, the results of this study also have the potential to help algorithm developers for tracing error characteristics and algorithm development.

II. MATERIALS AND METHODS

A. Study Area

The Yellow River Basin, the second largest basin in China, spans from the western part of the Bayan Kara Mountains to the east coast of the Bohai Sea, north to the Yinshan Mountains, and south to the Qinling Mountains. It covers a vast area of 7.52×10^5 km^2 (32.15°N–41.87°N, 95.87°E–119.07°E). The terrain in the basin is complex, with a general pattern of higher elevations in the west and lower elevations in the east. The western regions are mountainous, while the eastern regions are relatively flat. Precipitation exhibits low and uneven distribution patterns, with higher amounts of rainfall in the eastern regions and on the windward slopes of the mountain ranges, such as the northern slopes of the Qinling Mountains. Annual precipitation in these areas typically ranges from 700 to 1000 mm. In contrast, the deeply inland northwestern regions receive less than 150 mm of total annual precipitation.

The Yellow River Basin can be divided into three subbasins based on the natural environment and hydrology of the area through the river flows: the upper reaches, middle reaches, and lower reaches. The upper reaches stretch from the source of the river to the town of Toktor Hekou in Inner Mongolia. The middle reaches extend from Toktor Hekou to the vicinity of the Hua-yuan-kou at Taohuayu in Henan Province. Finally, the lower reaches encompass the area from Taohuayu to the estuary of the Yellow River. In this study, data were collected from 299 national meteorological stations within the Yellow River Basin. The distribution of these stations is illustrated in Fig. 1. The upper reaches of the Yellow River Basin have the most complex topography and the largest area, spanning 386 000 km^2. However, the number of meteorological stations in this region is relatively sparse, totaling 123. In the middle reaches, the topographical differences are reduced compared with the

upper reaches, covering a basin area of 344 000 km^2. This region has the largest number of meteorological stations, with a total of 150, primarily concentrated in the flat terrain of the low-altitude areas. The downstream region, located in the North China Plain, has the smallest basin area of approximately 23 000 km^2 and consists of 26 meteorological stations.

B. Datasets

1) Ground-Based Observations: Hourly ground-based basic meteorological observations provided by the China Meteorological Administration (CMA) were utilized as the reference data in this study. These observations can be accessed on the CMA website.[1] Rigorous quality control measures were applied to the precipitation observations from all meteorological stations [32]. These measures were implemented to ensure the accuracy and reliability of the data. The ground-based observations have been widely used as baseline data for evaluating the errors in SPEs [33], [34], [35].

To ensure the scientific integrity and credibility of this study, stations with missing precipitation data between September 2019 and September 2021 were excluded. Subsequently, hourly precipitation data from 299 meteorological stations, exhibiting 100% data availability throughout the study period, were selected as reference data.

2) IMERG Products: IMERG is a representative SPE provided by GPM. It offers global precipitation data with high temporal and spatial resolution, capturing intervals of 30 minutes in time and a spatial resolution of $0.1° \times 0.1°$ [36]. By integrating data from onboard microwave, infrared, rainfall radar, and other sensors, IMERG leverages the complementary advantages of multiple data sources.

To cater to various application needs and account for differences in data sources and latency, the IMERG system generates three algorithmic products. These include IMERG Early Run (IMERG_E) with a latency of 4 h, IMERG Late Run (IMERG_L) with a latency of 12 h, and IMERG Final Run (IMERG_F) with a latency of 3.5 months. The Final algorithmic product consists of two versions: IMERG_F_UnCal, which is uncorrected, and IMERG_F_Cal, which incorporates ground-based precipitation values using monthly-scale observations from the Global Precipitation Climatology Central (GPCC) stations.

Given the different time latency and application scopes of these algorithmic products (source is available online[2]), this article conducts a systematic analysis and quantification of the errors associated with IMERG_E, IMERG_L, IMERG_F_UnCal and IMERG_F_Cal. Table I presents the key characteristic parameters of these products.

C. Methods

1) Categorical Statistical Indices: To assess the ability of SPEs to detect precipitation events and understand the sources of errors, three categorical statistical indices are used: the

---

[1][Online]. Available: http://data.cma.cn
[2][Online]. Available: https://gpm.nasa.gov/data/directory

Satellite Product	Resolution	Latency	Data Source	Gauge Correction
IMERG_E	0.1°, 0.5h	4 h	PMW, IR	No
IMERG_L	0.1°, 0.5h	12 h	PMW, IR	No
IMERG_F_UnCal	0.1°, 0.5h	3.5 months	PMW, IR	No
IMERG_F_Cal	0.1°, 0.5h	3.5 months	PMW, IR	Yes

probability of detection (POD), misses (MIS), and false alarm rate (FAR) [36]. POD measures the proportion of precipitation events correctly detected by SPEs out of all actual precipitation events. It indicates the ability of SPEs to accurately identify and capture precipitation occurrences. MIS represents the proportion of precipitation events missed by satellites, relative to the total number of true precipitation events, and the instances where satellites failed to identify precipitation events. FAR measures the proportion of false precipitation events identified by satellites relative to the total number of true precipitation events. All the categorical indices mentioned above have values ranging from 0 to 1. To account for the temporal resolution of 1 h and minimize the impact of light precipitation, a threshold of 0.1 mm/h is commonly used to determine whether precipitation occurs or not

$$\text{POD} (\%) = \frac{N\{(S_i \geq t) \text{ and } (G_i \geq t)\}}{N\{(G_i \geq t)\}} \times 100 \quad (1)$$

$$\text{FAR} (\%) = \frac{N\{(S_i \geq t) \text{ and } (G_i < t)\}}{N\{(S_i \geq t)\}} \times 100 \quad (2)$$

$$\text{MIS} (\%) = \frac{N\{(S_i < t) \text{ and } (G_i \geq t)\}}{N\{(G_i \geq t)\}} \times 100. \quad (3)$$

Note: where S_i and G_i are the hourly precipitation estimated by satellite-based precipitation products and gauge observations, respectively; N means the number of hours for different conditions; and t represents the hourly precipitation threshold.

2) Error Component Method: In this study, the error component method [21] is utilized to decompose the total bias into three distinct components: hit bias, missed bias, and false bias (Table II in the Appendix). Hit bias occurs when both SPEs and gauge observations detect a precipitation event, but the estimated precipitation volume differs. Hit bias can have either a positive or negative bias indicating an overestimation or underestimation of precipitation, respectively. Missed bias refers to a gauge-observed precipitation event that is not detected by SPE. This results in missed precipitation and the missed bias component is always negative since it represents the absence of detected precipitation. False bias arises when SPE detects rainfall features that are not present in reality, leading to misdetected precipitation [24], [37]. False bias is always positive, indicating the presence of falsely identified precipitation

$$\text{Total bias (mm)} = \sum (S_i - G_i) \quad (4)$$

$$\text{Hit bias (mm)} = \sum (S_i - G_i)$$
$$\text{when } (S_i \geq t) \text{ and } (G_i \geq t) \quad (5)$$

$$\text{Missed bias (mm)} = \sum (S_i - G_i)$$
$$\text{when } (S_i < t) \text{ and } (G_i \geq t) \quad (6)$$

$$\text{False bias (mm)} = \sum (S_i - G_i)$$
$$\text{when } (S_i \geq t) \text{ and } (G_i < t). \quad (7)$$

It is noted that these three bias components may offset each other, resulting in a total bias that is smaller than the magnitude of any individual component. This error decomposition scheme is employed to evaluate the accuracy of estimating precipitation amounts [23].

3) Multiplicative Model: To enable more precise quantification of the error, the multiplicative model is used to further track the systematical and random bias in the hit bias [24]. With this approach, the error can be quantified more accurately

$$S_i = \alpha G_i^b e^{\varepsilon_i} \quad (8)$$

where α is the offset and b is the scale parameter. The parameters α and b together determine the systematic error. The random error is denoted by ε, which represents the random error with a zero mean and variance of σ^2. For ease of computation, the original equations are log-transformed as follows:

$$\ln(S_i) = \alpha + \beta \ln(G_i) + \varepsilon_i \quad (9)$$

where α ($\alpha = \ln\alpha$) is the offset parameter used to shift *Gi* PDF to the left ($\alpha < 0$) or the right ($\alpha > 0$); β ($\beta = b$) refers to the scale parameter used to enlarge ($\beta > 1$) or shrink ($\beta < 1$) *Gi* PDF; and σ gives the result of the addition of the random error uniformly enlarging the PDF. Thus, α and β can reflect systematic errors, while σ reflects random errors. These three parameters are calculated using (9) and ordinary least squares. For a more detailed explanation of this multiplicative error model, the reader is referred to Tang et al. [24].

III. RESULTS

A. Evaluation of Seasonal-Scale Precipitation Errors

Fig. 2 illustrates the spatial distribution of mean daily precipitation in the Yellow River Basin across different seasons. The general pattern shows higher precipitation levels in the southeast and lower levels in the northwest [see Fig. 2(a)]. Among the seasons, winter and spring exhibit lower precipitation, while summer and autumn experience more abundant precipitation. IMERG_E, IMERG_L, IMERG_F_UnCal, and IMERG_F_Cal can effectively capture the seasonal variations in precipitation in the Yellow River Basin. The spatial distributions of these SPEs align closely with the observed data from gauge observations. This demonstrates the notable advantage of IMERG SPEs in accurately representing the spatial distribution pattern of precipitation. However, it is important to acknowledge that there are variations in the accuracy of precipitation estimation among different IMERG SPEs. While they generally reflect the spatial
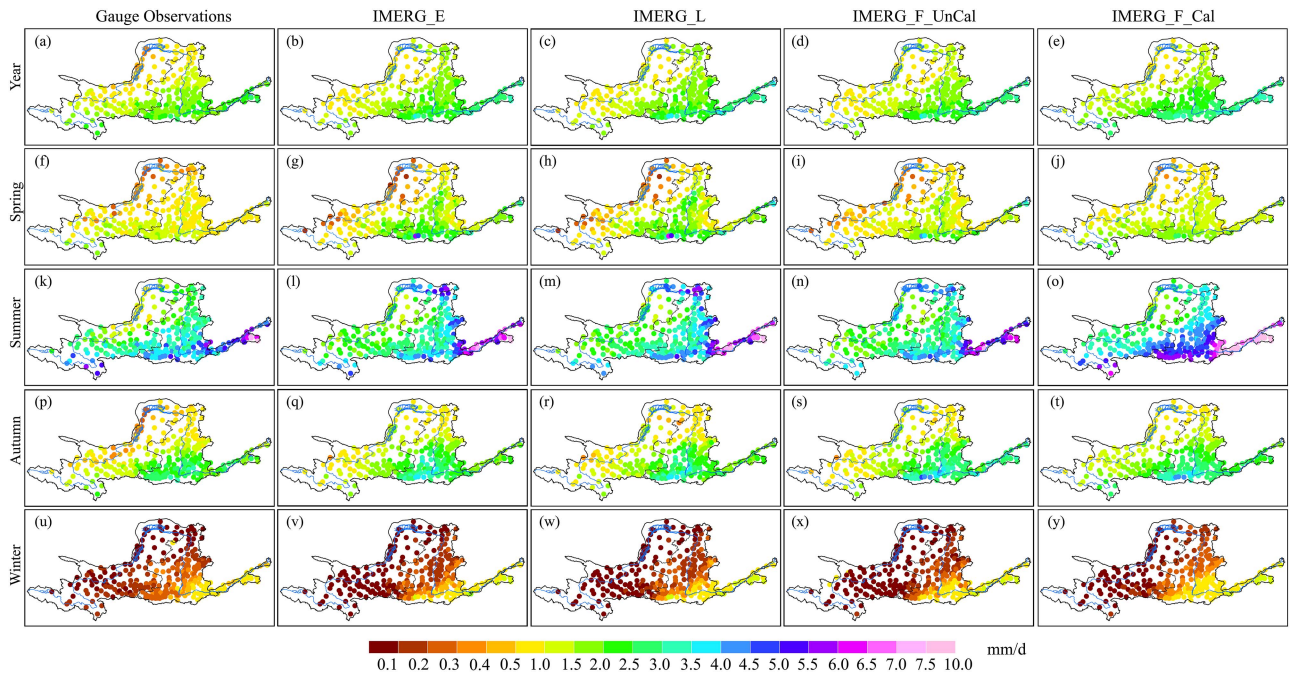
Fig. 2. Spatial distribution of annual average precipitation and seasonal daily mean precipitation in the Yellow River Basin for observed station data (column 1) and four IMERG SPEs (columns 2 to 5) from 2019 to 2021. The seasons are defined as follows: March to May (spring), June to August (summer), September to November (autumn), and December to February (winter). The four IMERG SPEs are as follows: IMERG_E (b, g, l, q, v), IMERG_L (c, h, m, r, w), IMERG_F_UnCal (d, i, n, s, x), and IMERG_F_Cal (e, j, o, t, y).

distribution pattern well, there may be differences in their ability to precisely invert the accuracy of precipitation.

Based on the combined analysis of the spatial distribution (see Fig. 2) and density scatterplot (see Fig. 3), several observations can be made. All four IMERG SPEs tend to overestimate precipitation in spring, summer, autumn, and winter. Among them, IMERG_F_Cal exhibits the highest inversion accuracy, showing the best agreement with gauge observations, especially in terms of CC and RMSE [see Fig. 3(m)–(p)]. In spring, IMERG_E and IMERG_L have different degrees of precipitation underestimation in areas on both sides of the upper Yellow River [see Fig. 2(g) and (h)], while IMERG_F_UnCal does not exhibit this issue [see Fig. 2(i)]. Despite a more substantial overestimation error, IMERG_F_Cal, after gauge correction, demonstrates better data accuracy than the other three IMERG products as evidenced by CC, RMSE, and the degree of data fit [see Figs. 2(j) and 3(m)]. During summer, all four SPEs show a tendency to overestimate precipitation [see Fig. 2(k)–(o)], with IMERG_F_Cal also overestimating downstream precipitation [see Fig. 3(n)]. In autumn, IMERG_F_Cal displays the highest correlation coefficient (CC = 0.71), the lowest root mean square error (RMSE = 4.12 mm/d) [see Fig. 3(o)], and the best agreement with gauge observations. In winter, all four SPEs suffer from underestimation of upstream precipitation and overestimation of downstream precipitation [see Fig. 2(u)–(y)].

Based on the spatial distribution shown in Fig. 2, notable overestimation and underestimation of precipitation can be observed in specific areas of the Yellow River Basin across the four IMERG SPEs. To further analyze the error characteristics during the summer season, three representative areas were selected for in-depth examination. These areas include the northern part of

the Yellow River Basin, the southwestern part of the source area of the Yellow River, and the southeastern part—the northern slope of the Qinling Mountains and the three areas are denoted as I, II, and III in Fig. 11 in the Appendix.

In Area I, there is a significant overestimation of precipitation by IMERG_E, IMERG_L, and IMERG_F_UnCal, with an average overestimation error of approximately 2.0 mm/d. However, IMERG_F_Cal, after being corrected using the GPCC dataset, aligns closely with the gauge observations, effectively addressing the overestimation issues. Conversely, in Area II, the three IMERG SPEs tend to underestimate precipitation, while IMERG_F_Cal demonstrates better agreement with the observed data for this region. However, in Area III (see Fig. 11 in the Appendix), IMERG_F_Cal exhibits a significant overestimation of precipitation, averaging an error of 2.17 mm/d. This phenomenon may be caused by the uncertainties from the gauge correction algorithms, such as the overestimation of the GPCC, which is used in the generation of IMERG_F_Cal [38]. Interestingly, all four IMERG SPEs consistently exhibit substantial overestimation of seasonal precipitation near the Yellow River. This overestimation pattern persists across all four seasons (see Fig. 2), with the highest magnitude observed during the summer season, and this overestimation error over the inland water bodies is caused by the deficiencies of PMW-based retrievals for emissivity characterization [37] (see Fig. 11 in the Appendix).

The observed phenomenon can be attributed to the following reasons.

1) Sparse and uneven distribution of surface observation stations in the Inner Mongolia Plateau region may lead to significant deviations between the precipitation data
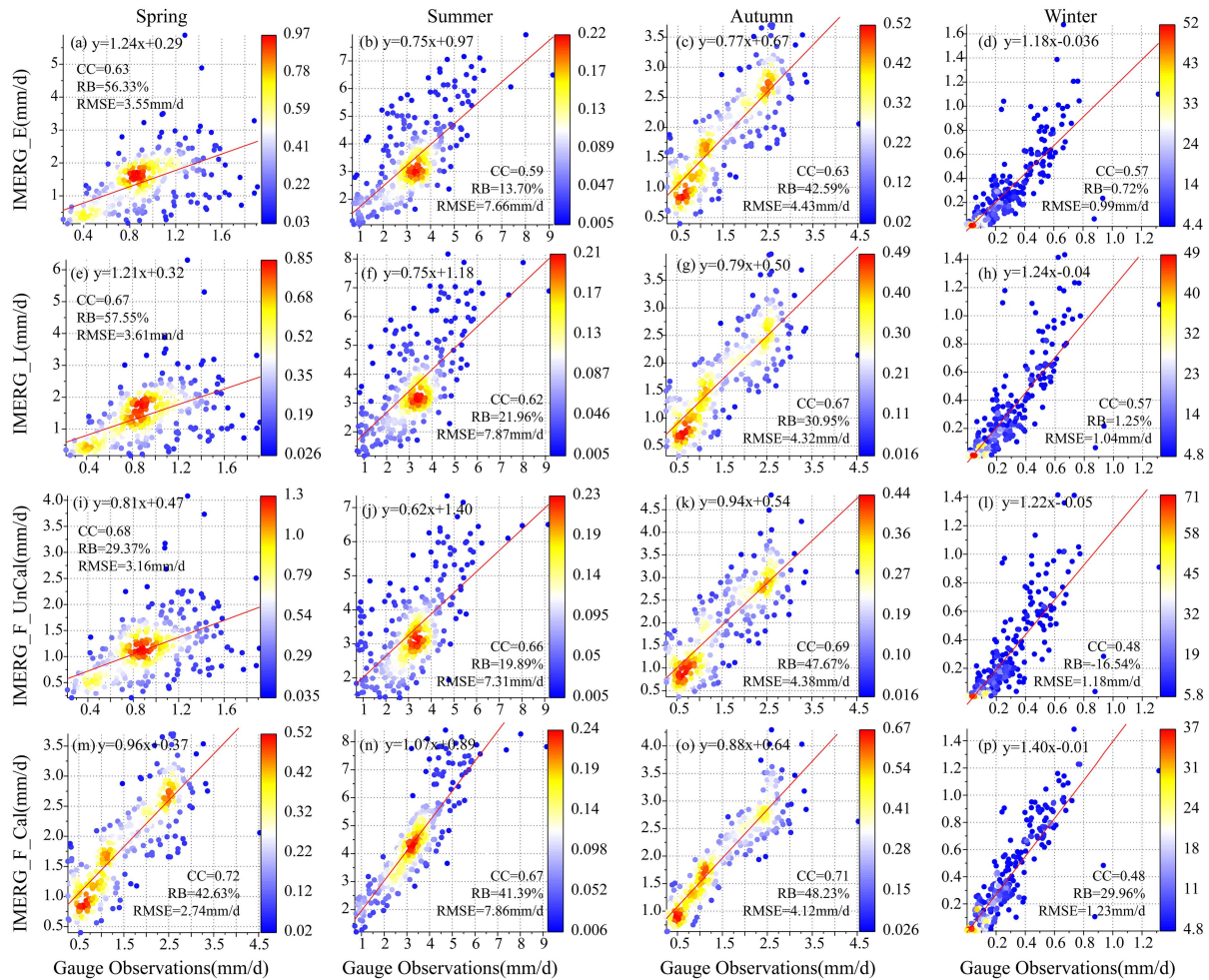
Fig. 3. Scatter density plots depicting the seasonal mean daily precipitation in the Yellow River Basin from 2019 to 2021, comparing the observed station with the four IMERG SPEs. The plots include fitted lines (shown in red) representing the relationship between the four SPEs and observed stations. Continuous statistical indicators (RB, CC, and RMSE) are provided. The colored bands within the plots represent the scatter densities of the data points.

measured by the SPEs and gauge observations. These stations have limited coverage and lack representativeness.

2) The presence of overestimation of precipitation over inland pixels containing small water bodies, such as rivers, lakes, and reservoirs. These anomalies are caused by the poor characterization of the differences in emissivity and temperature of water surfaces in the PMW frequencies used by the retrievals. The PMW retrievals are known to be sensitive to land surface heterogeneity, including contrasts in temperature and emissivity [23], [37], [39].

3) For regions with high altitudes and complex terrain, data evaluation contains considerable uncertainty resulting from the biases of ground observations and the errors in the resampling and interpolation algorithms [15], [40], [41], [42].

4) During the production process of IMERG_F_Cal, the gauge correction algorithms or the overestimation of GPCC may introduce overcorrection issues in localized areas, leading to the observed discrepancies.

All four SPEs of IMERG can effectively capture the spatial distribution and seasonal characteristics of precipitation in the Yellow River Basin. They depict low precipitation in winter and

spring, and high precipitation in summer and autumn. However, these SPEs exhibit varying degrees of precipitation inversion bias in different seasons, generally tending to overestimate precipitation. Among them, IMERG_F_Cal demonstrates the highest accuracy and stability in precipitation reversion. While there are overestimation errors in certain regions with complex terrain, further algorithm refinement can enhance the accuracy of precipitation inversion in these areas. It is worth noting that IMERG_E and IMERG_L exhibit significant overestimation issues at the two stations in the southern part of the middle reaches of the Yellow River Basin [see Fig. 2(g)–(h)]. However, this overestimation problem is not present in IMERG_F_Uncal and IMERG_F_Cal [see Fig. 2(i)–(j)]. This discrepancy may be attributed to the observation correction procedure included in the IMERG_F algorithm, which effectively corrects the overestimation error in this region [see Fig. 2(i)–(j)].

B. Occurrence Analysis

The ability to accurately detect precipitation events is a crucial factor in the inversion of precipitation using SPEs. In this section, the detection capability of four selected IMERG SPEs was
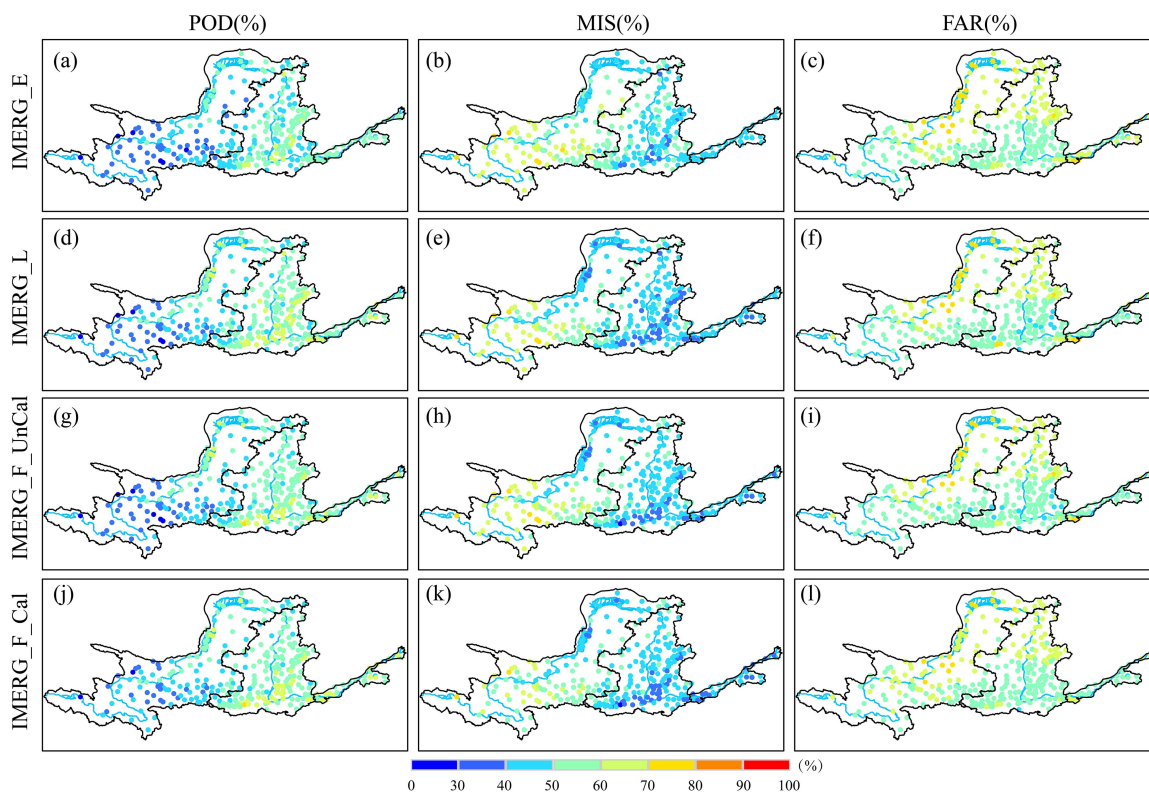
Fig. 4. Spatial distribution of each categorical statistical index (POD, MIS, FAR) at the hourly scale of IMERG SPEs. IMERG_E (a, b, c); IMERG_L (d, e, f); IMERG_F_UnCal (g, h, i); IMERG_F_Cal (j, k, l), respectively. It should be noted that the 0.1 mm/h rain/no rain threshold is used here.
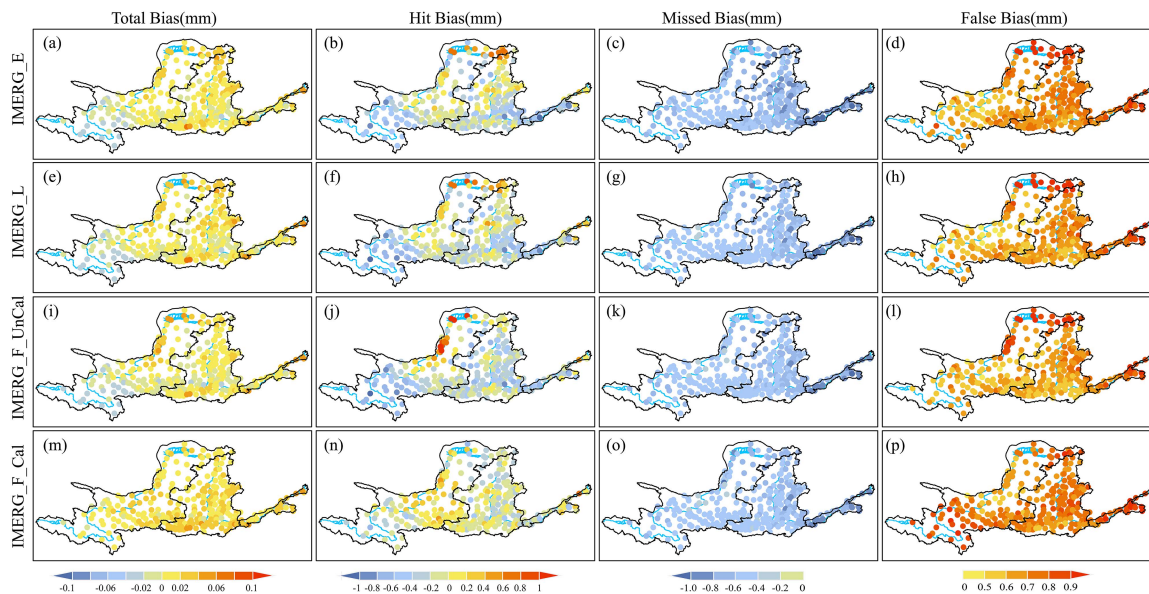

Fig. 5. Spatial distribution of error components at hourly scales for IMERG SPEs.

evaluated on an hourly time scale. Three metrics, namely POD, FAR and MIS are utilized to evaluate their performance.

Fig. 4 illustrates the spatial distribution of categorical statistical indicators for the four IMERG SPEs, highlighting notable differences in their capabilities for precipitation events. Among the four SPEs, IMERG_F_Cal exhibits the best overall performance, with the highest regional average pod rate (POD = 52.7%) and the lowest miss rate (MIS = 47.3%). However, it is worth noting that IMERG_F_Cal also displays a high false alarm rate (FAR = 59.2%), corresponding to the aforementioned overestimation of precipitation by IMERG_F_Cal [see Fig. 2(e)]. On the other hand, IMERG_F_UnCal demonstrates the lowest average false alarm rate (FAR = 58.1%). IMERG_L ranks second after IMERG_F_Cal in detecting precipitation
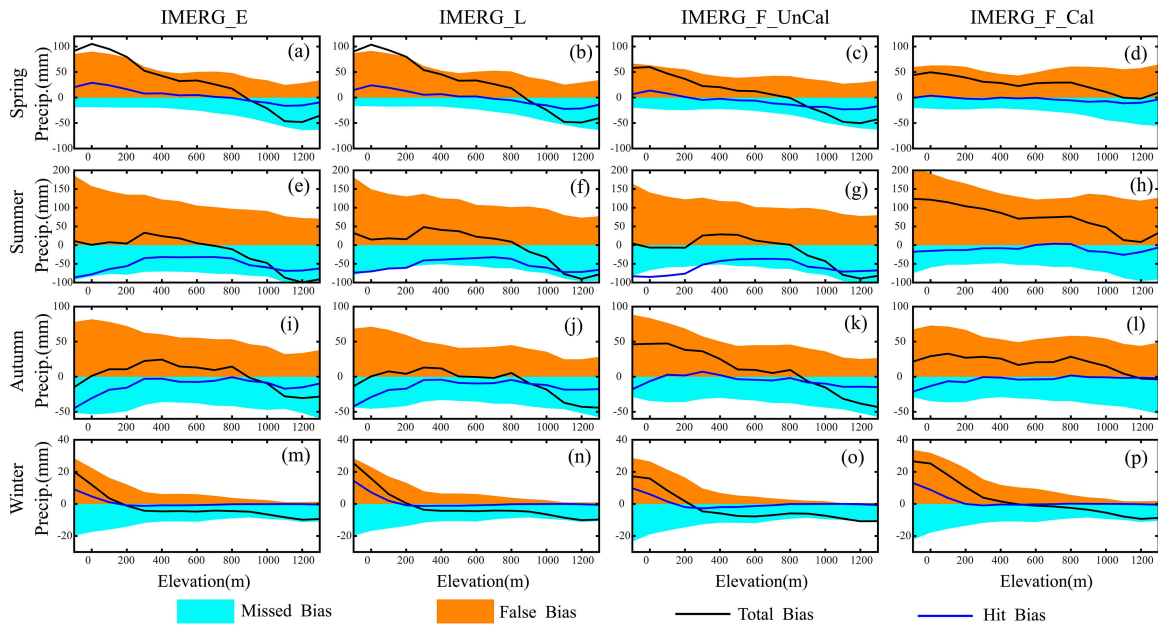
Fig. 6. Schematic representation of total bias and error components with elevation for IMERG SPEs in (a)–(d) spring, (e)–(h) summer, (i)–(l) autumn, (m)–(p) and winter.
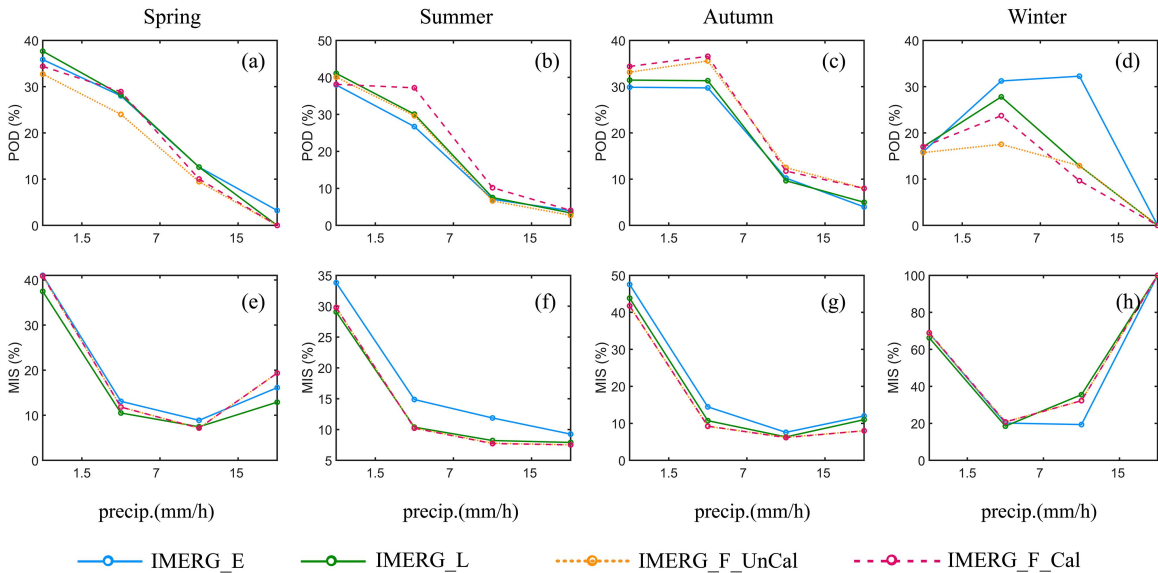

Fig. 7. Classification indicators of hourly precipitation for the IMERG SPEs over the Yellow River Basin with different intensities. Note that different y axis limits are used in Fig. 7.

events, while IMERG_E exhibits the poorest performance with the lowest mean POD (48.7%), the highest mean MIS (51.3%), and the highest mean FAR (60.0%) among all the SPEs.

In the lower reaches of the Yellow River Basin, the four IMERG SPEs consistently exhibit a high regional mean POD ranging from 54.6% to 58.8% and a low regional mean MIS ranging from 41.2% to 45.4%. These favorable results can be attributed to the flat terrain in the lower reaches, where precipitation is less affected by topography and geomorphology. On the contrary, the upstream area situated on the Tibetan Plateau is characterized by complex terrain, and perennial snow cover in the local mountainous areas, precipitation in this region may be largely affected by subsurface conditions and topography.

Consequently, the detection accuracy of satellite sensors in this region is greatly disturbed. In the upstream area, all four SPEs exhibit low POD values ranging from 42.7% to 46.6%, high MIS values ranging from 53.4% to 57.3%, and high FAR values ranging from 60.0% to 61.7%. Among the four SPEs, IMERG_F_Cal demonstrates the best overall performance, exhibiting the highest ability to detect precipitation events in all areas.

The ability of IMERG SPEs to detect precipitation events exhibits distinct seasonal characteristics. During the summer season, which is characterized by heavy and concentrated precipitation (see Fig. 13 in the Appendix), the four IMERG SPEs demonstrate different detection capabilities compared to the
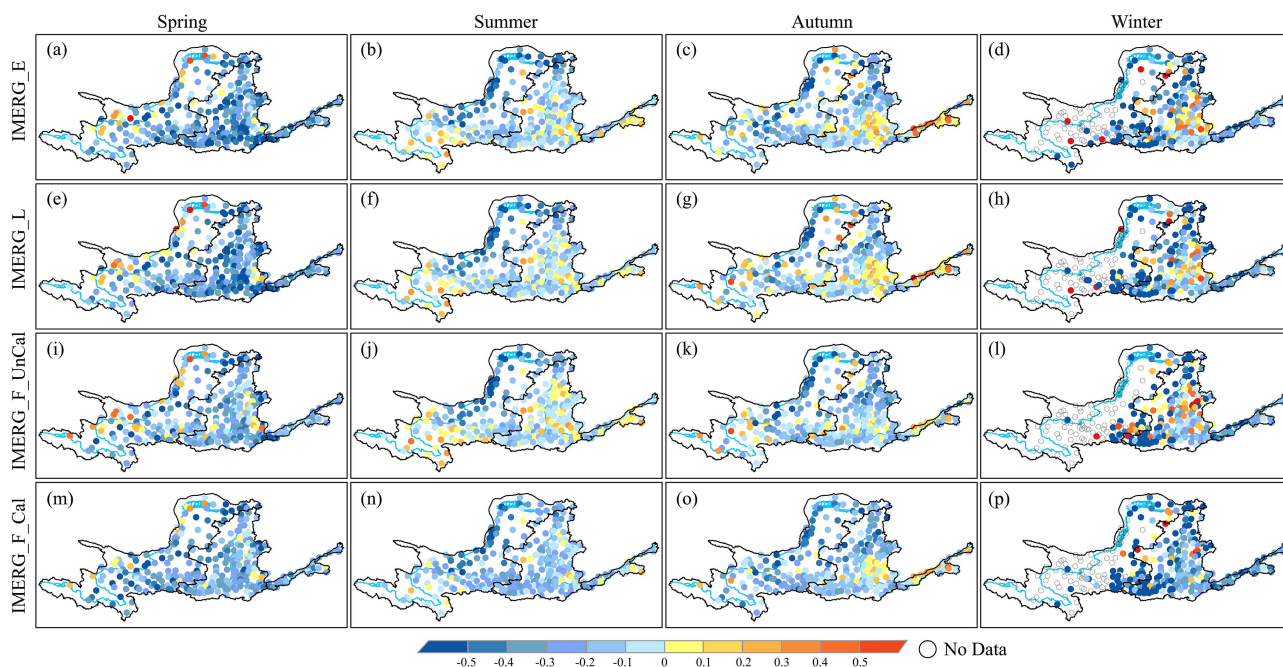
Fig. 8. Spatial distribution of the scale parameter α for IMERG SPEs in the four seasonal error models for spring (column 1) summer (column 2) autumn (column 3) and winter (column 4). The closer the value of the scale parameter α is to zero, the smaller the offset error is. Blank parts of the stations represent areas of missing data.
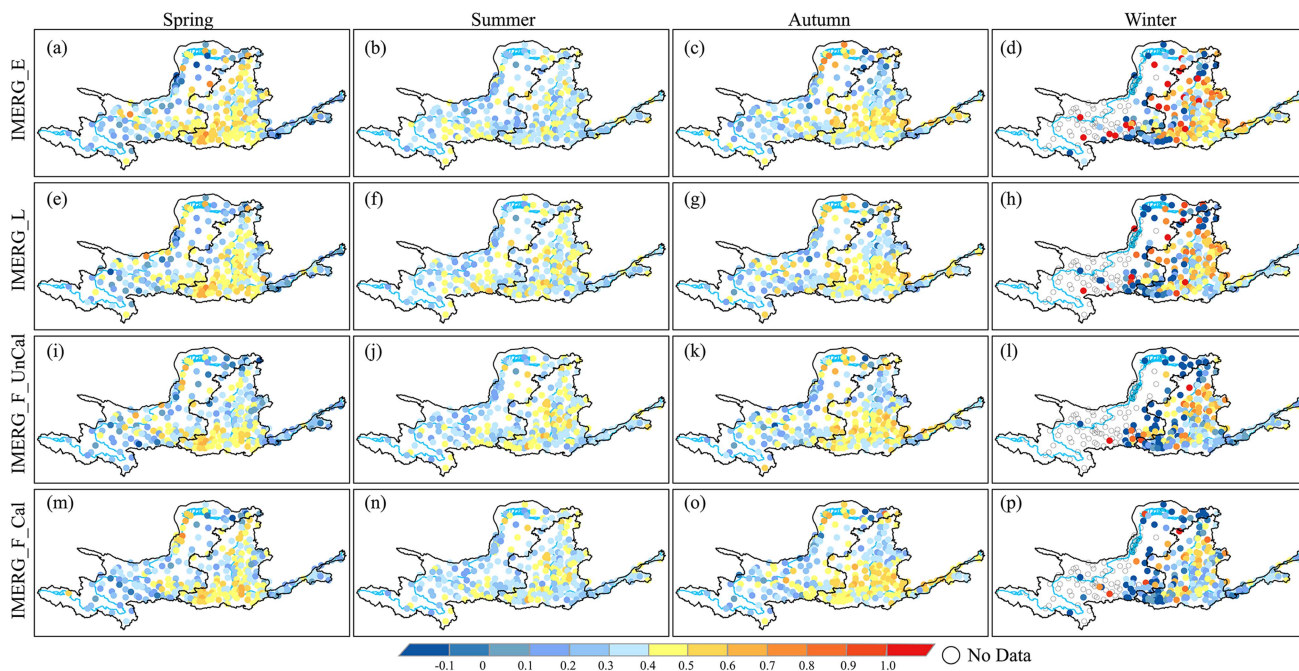

Fig. 9. Spatial distribution of the scale parameter β for IMERG SPEs in the four seasonal error models for spring (column 1) summer, (column 2) autumn, (column 3), and winter (column 4). The closer the value of the scale parameter β is to 1, the lower the shape error. Blank parts of the stations represent areas with missing data.

spring season (see Fig. 12 in the Appendix). In terms of POD and MIS, both products of the IMERG_F algorithm exhibit notable advantages, particularly the remarkable correction effect observed in IMERG_F_Cal. In the midstream area, IMERG_F_Cal achieves a high POD value of 67.3%. During autumn (see Fig. 14 in the Appendix), IMERG_F continues to exhibit a

clear advantage, particularly in the southern part of the middle reaches of the Yellow River Basin and throughout the lower reaches, resulting in a decrease in the mean MIS value from 52.9% to approximately 39.0%. However, the performance of IMERG precipitation products is the poorest during the winter season (see Fig. 15 in the Appendix). The four SPEs exhibit
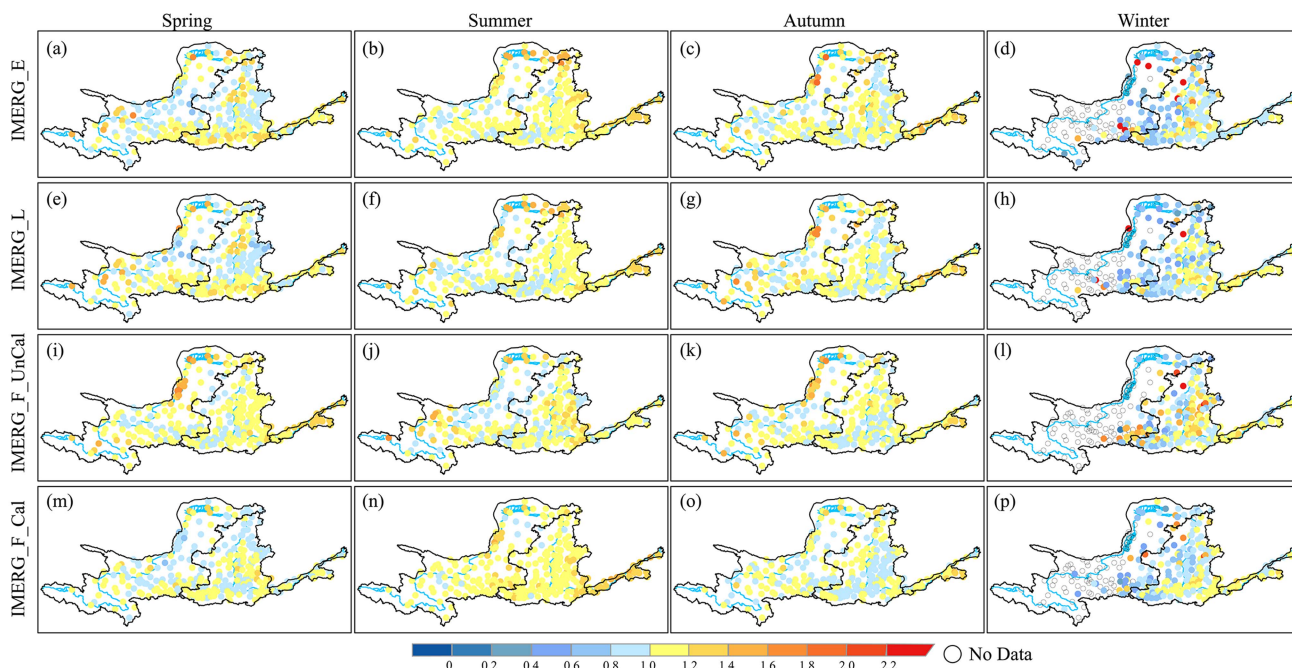
Fig. 10. Spatial distribution of the random error parameter σ, which represents the standard deviation of the random error (mm/h), in the four seasonal error models of IMERG SPEs for spring (column 1), summer (column 2), autumn (column 3), and winter (column 4). A lower value of the random error parameter σ represents a smaller random error. Blank parts of the stations represent areas with missing data.

low POD, high MIS, and high FAR values. In the upstream region, the regional average POD for the four SPEs remains low ranging from 4.61% to 7.05%. Notably, IMERG_F_UnCal performs poorly in monitoring winter precipitation, with high FAR and MIS values reaching 60% to 100%. This may be due to the fact that winter precipitation often occurs in solid form, such as snow or ice particles, and therefore the accuracy of PMW retrieval of precipitation is hampered. This finding aligns with the results reported by Moazami and Najafi [18], Wu et al. [43], and other researchers [17], [21], [44].

In summary, the four SPEs exhibit significant variations in their ability to detect precipitation events. IMERG_F_Cal demonstrates the best overall performance, followed by IMERG_L, while IMERG_E performs the worst. Moreover, the detection capabilities of the four IMERG SPEs vary across different regions of the Yellow River Basin. The downstream region shows the highest detection capability, followed by the midstream region, while the upstream region exhibits relatively lower effectiveness. The precipitation frequency error also plays a crucial role in the overall precipitation error. In addition, there are seasonal differences in the performance of the IMERG algorithm in monitoring precipitation events, followed by spring and autumn, while its performance is the least accurate during winter.

C. Error Components Analysis

In the previous part of the error evaluation, we identified the precipitation frequency error as a significant factor contributing to the overall precipitation volume error. To gain further insights

into the sources of precipitation errors related to different monitoring occasions, we adopt the error component method. This method allows us to break down the total bias into three error components: hit bias, missed bias, and false bias. Fig. 5 displays the spatial distribution of the total bias and these three error components.

As can be seen from Fig. 5(a), (e), (i), and (m), the values of total bias in all cases are relatively small, ranging from 0.006 to 0.018 mm/h. These values are significantly smaller than the sum of the three error components. This can be attributed to the presence of both positive and negative error components, which can offset each other. It highlights the importance of considering precipitation events and analyzing precipitation error components rather than relying solely on the traditional total bias for evaluating SPEs [3], [45].

The spatial distribution of total bias across the four IMERG SPEs is similar. Fig. 5(m) illustrates that IMERG_F_Cal demonstrates a more stable overall performance. Its total bias values show no significant variation among the three sub-basins of the Yellow River Basin and remain within the range of 0–0.02 mm. On the other hand, IMERG_E, IMERG_L and IMERG_F_UnCal exhibit lower total bias values in the Yellow River source area. However, their individual error components are larger, indicating a less consistent performance.

The spatial distribution of missed bias showed little overall difference in all four SPEs. In the upper and middle reaches, the missed bias remained relatively constant, ranging from −0.5 to −0.6 mm. However, in the lower reaches, the missed bias increased significantly to around −0.8 mm. It is worth noting that missed bias emerges as the primary source of error during winter for all four SPEs (see Fig. 16 in the Appendix). This may

be related to the challenges of using PMW measurements to accurately estimate snow or precipitation on snow or ice-covered surfaces. In addition, winter precipitation in these regions may be associated with low levels of cloudiness and warm rain processes that may not involve significant ice particles. These factors contribute to the higher missed bias values observed during winter. The variations in missed bias among the four SPEs could be attributed to differences in their screening strategies for terrestrial pixels [21]. These strategies play a role in determining which pixels are classified as precipitation events and which are not, affecting the accuracy of precipitation detection.

The values of the three error components can have positive or negative values that can potentially cancel each other out [21]. Missed bias is negative, false bias is positive, and hit bias values can be positive or negative. In this study, most of the hit bias predominantly exhibits negative values. Despite the negative values of missed bias and hit bias, the total bias of all four SPEs shows an overestimation of precipitation. This suggests that false bias plays a dominant role in the overall precipitation error. Furthermore, differences in the spatial distribution of false bias are observed among the four SPEs. Specifically, the IMERG_F_Cal exhibits the lowest false bias values in the northern part of the Yellow River Basin but has higher false bias in the Yellow River source area, as well as in most of the middle and lower reaches [see Fig. 5(d), (h), (l), and (p)]. On the other hand, IMERG_E, IMERG_L, and IMERG_F_UnCal show high hit bias in the northeastern part of the upper Yellow River Basin and along the Yellow River [see Fig. 5(b), (f), and (g)], deviating from the actual precipitation. However, IMERG_F_Cal does not exhibit this pattern. Although IMERG_F_Cal performs better in terms of hit bias and missed bias, its larger false bias contributes to its predominantly overestimated total bias. This finding effectively explains the previously observed precipitation overestimation errors (see Fig. 2) for the four IMERG SPEs in the vicinity of the Yellow River, mainly attributed to false bias and hit bias.

D. Elevation-Dependent Bias Analysis

In this subsection, the degree of elevation dependence of the error components is further assessed. The elevation-dependent bias analysis was conducted at seasonal scales (see Fig. 6).

The results from Fig. 6 indicate that the total bias and error components of the four SPEs exhibit clear topographic dependence, with the magnitude of the error components varying with the elevation. However, the absolute values of total bias are relatively smaller compared to the absolute values of the three error components. The sum of absolute values of the three components is significantly higher than the absolute total bias due to the presence of positive and negative error components that can cancel each other out. This finding is consistent with the observations from the spatial distribution of the error components in the previous section (see Fig. 5). Once again, this phenomenon emphasizes the importance of not relying solely on total bias for evaluating the error characteristics of SPEs, as it may lead to an evaluation that is more favorable than the actual performance.

Based on the analysis of the seasonal cumulative error components and their dependence on topography [Fig. 6(a)–(p)], it is observed that the elevation dependence of the error components for the four SPEs exhibits a distinct seasonal pattern (see Fig. 6). The total bias exhibits a tendency to underestimate the precipitation occurrence in high elevations and overestimate precipitation in low elevations, which is consistent with the findings of Hong et al.'s [46] study. In spring, the absolute values of missed bias for all SPEs [see Fig. 6(e)–(h)] increase with higher elevation. In addition, the absolute values of total bias and hit bias for IMERG_E, IMERG_L and IMERG_F_UnCal show a decreasing trend followed by an increasing trend as elevation increases. Notably, these values change from positive to negative within the elevation range of 800–1000 m. On the other hand, the false bias of IMERG_E, IMERG_L, and IMERG_F_UnCal decreases with increasing elevation. In contrast, the False Bias of IMERG_F_Cal remains relatively stable with minimal fluctuation overall.

In the summer season, the absolute values of the error components are significantly higher compared with the spring. This can be attributed to the higher amount of precipitation during the summer, which is consistent with the precipitation distribution shown in Fig. 2(k)–(o). The Hit Bias is consistently negative for all four SPEs. IMERG_F_Cal tends to predominantly overestimate precipitation during the summer months. On the other hand, IMERG_E, IMERG_L, and IMERG_F_UnCal tend to predominantly overestimate precipitation in the elevation range of 0–800 m, and underestimate precipitation in elevation ranges greater than 800 m.

In the autumn season, the absolute values of each error component are reduced compared with the summer season, typically ranging between −50 and 100 mm. The four SPEs transition from overestimating to underestimating precipitation in the elevation range of 800–1000 m. Similar to the summer season, the Hit Bias for four SPEs remains overwhelmingly negative. It can be inferred that False Bias dominates the error components of the four SPEs when the elevation is below 800 m.

In winter, the absolute values of Missed Bias decrease with increasing elevation. The total bias and hit bias of IMERG_E, IMERG_L and IMERG_F_UnCal are positive in the elevation range of 0–200 m and then change from positive to negative after the elevation exceeds 200 m. Since the absolute value of missed bias is greater than the absolute value of hit bias, it can be inferred that missed bias is the primary source of error for IMERG_E, IMERG_L, and IMERG_F_UnCal during winter at elevations above 200 m. In addition, Fig. 6(p) indicates that missed bias is also the main source of error for IMERG_F_Cal in winter when the elevation is above 500 m.

In summary, the analysis reveals that the total bias and error components of the four SPEs exhibit significant elevation dependence. False bias is identified as the dominant error component for IMERG_F_Cal. The specific characteristics of the four error components vary across different seasons. In spring, summer, and autumn seasons at elevations below 800 m, false bias is identified as the main source of error for IMERG_E, IMERG_L, and IMERG_F_UnCal. However, during winter, the primary source of error for these three SPEs at elevations above 200

m shifts to missed bias. Similarly, for IMERG_F_Cal in winter, missed bias becomes the main source of error at elevations over 500 m. We note that the failed detection of precipitation in winter, presumably snowfall, is mostly due to the intrinsic inability to retrieve precipitation with PMW when the underlying land surface is covered by snow or ice [21].

In light of these findings, we recommend that future research endeavors prioritize the reduction of false bias, integration of snowfall retrievals, and advancement of methods for merging gauge and satellite precipitation data. Enhanced snowfall detection capabilities in these products will also hold paramount importance for land surface hydrological studies concerning snowpack accumulation and melting.

E. Intensity-Dependent Detection Error Analysis Precipitation

In the previous section, we observed variations in error components for IMERG SPEs across different seasons. We speculated that these differences might be influenced by precipitation intensity. Therefore, precipitation this section, we evaluate the impact of different precipitation intensities on the identification of precipitation events by IMERG SPEs in four seasons, as illustrated in Fig. 7. We classify precipitation into four thresholds, corresponding to light, moderate, heavy and storm precipitation [47]. It is important to note that the determination of precipitation intensity thresholds relies on ground-based precipitation observations. As a result, the calculation of FAR (false alarms of IMERG SPEs when ground-based site observed no precipitation event) for different precipitation intensities is not feasible. Therefore, this section focuses solely on the analysis of POD and MIS.

In general, there is a strong correlation between the ability of IMERG SPEs to capture precipitation events and precipitation intensity. Except for the winter season, under the same precipitation threshold, the IMERG SPEs exhibit high consistency in capturing precipitation events [see Fig. 7(a)–(d)]. The POD values of IMERG SPEs are generally below 40%, with the highest values observed during the summer season [see Fig. 7(b)], while the winter season shows the least ideal performance [see Fig. 7(d)]. As precipitation intensity increases, there is a general downward trend in POD. Among the four IMERG SPEs, they exhibit the poorest performance in capturing heavy and storm precipitation events, which aligns with the findings of Gan et al [47]. The low POD values (10%) indicate IMERG SPEs have relatively high incidences of misjudgment in capturing the intensity of precipitation, even though they could effectively detect of precipitation events (see Fig. 4). It is worth noting that this could be partially attributed to the limited sample size of intense precipitation events. In the case of light precipitation, IMERG SPEs exhibit the highest POD, indicating their relatively better ability to identify and detect light precipitation events [1], [14]. Among the four IMERG SPEs, IMERG_F_Cal demonstrates the highest overall POD, particularly during the summer and autumn seasons, indicating its superior capability in capturing precipitation events. This finding aligns with the previous analysis (see Figs. 13 and 14 in the Appendix).

IMERG SPEs exhibit the lowest MIS values ($<35\%$) in summer while highest MIS values ($>90\%$) in winter [see Fig. 7(e)–(h)]. This phenomenon can be attributed to the deficiency of PMW sensor and lower capability of IR sensor in accurate retrieving precipitation events on ice/snow surfaces [19], [48]. The high MIS values in winter could provide direct explanation for the previously mentioned phenomenon that the miss bias is the primary source of error during the winter season [see Fig. 16(c), (g), (k), and (o)]. In addition, IMERG SPEs also exhibit relatively higher MIS for light precipitation events during the spring, summer, and autumn seasons. Consequently, these misdetection of light precipitation events may lead to the underestimation of the amount of light precipitation events by IMERG SPEs [18].

Among the four IMERG SPEs, IMERG_E exhibits the highest overall missed detection rate, while IMERG_F demonstrates the lowest. Furthermore, the performance of IMERG_F_Cal (red line) and IMERG_F_UnCal (orange line) is almost indistinguishable, indicating that the GPCC bias correction procedure in the IMERG_F_Cal algorithm has limited effectiveness in rectifying missed detections of precipitation events in IMERG_F.

F. Multiplicative Model Analysis of Hit Bias

To quantitatively assess the Hit Bias, three parameters of the multiplicative model were evaluated in this section. The evaluation process considered only precipitation events with intensities exceeding 0.1 mm/h to avoid being influenced by trace amounts of precipitation. It is important to note that the challenging and variable terrain, high altitude, and harsh climatic conditions of the Tibetan Plateau resulted in null values for the three parameters α, β, and σ in the upper Yellow River basin during winter.

Fig. 8 provides the spatial distribution of parameter alpha (α) for the SPEs in spring, summer, autumn, and winter. A value of α closer to zero indicates a smaller systematic error. The figure demonstrates a clear seasonal variation in the spatial distribution of α, with the best performance observed during summer and autumn ($\alpha = -0.15$), followed by spring ($\alpha = -0.23$), and the worst performance occurring in winter ($\alpha = -0.29$). In spring, for most of the middle reaches of the Yellow River Basin, IMERG_E and IMERG_L exhibit predominantly negative α values, with values lower than -0.5. IMERG_F, on the other hand, has α values between -0.2 and 0, indicating a significantly better systematic error compared with IMERG_E and IMERG_L. Furthermore, the α values for IMERG_E, IMERG_L, and IMERG_F_UnCal exceed 0.5 at the Yellow River in the upper reaches of the basin. However, after being corrected by the ground stations, IMERG_F_Cal has α values ranging from 0 to 0.3, resulting in a substantial reduction in systematic error [see Fig. 8(a), (e), (i), and (m)]. In summer, the systematic errors of IMERG_F_Cal in the source area of the Yellow River and the middle reaches transition from positive to negative values, indicating an overall reduction in systematic errors [see Fig. 8(b), (f), (j), and (n)]. During the winter season [see Fig. 8(d), (h), (l), and (p)], although the α values for the four SPEs are not stable, it can be observed

that IMERG_F_Cal consistently exhibits the lowest and most stable systematic error. The overall comparison of the four SPEs suggests that IMERG_F_Cal demonstrates the most stable α value, followed by IMERG_F_UnCal, indicating that IMERG_F is relatively less affected by systematic errors.

Fig. 9 illustrates the spatial distribution of beta (β) for the SPEs during the four seasons. Beta along with alpha (α), represents the systematic error, where an optimal value of 1 indicates that the SPEs and the reference data have the same dynamic range. Based on the spatial distribution of β, summer and autumn exhibit consistent and stable performance, with autumn showing the best results ($\beta = 0.37$) [see Fig. 9(c), (g), (k), and (o)], while winter demonstrates the least favorable results ($\beta = 0.20$) [see Fig. 9(d), (h), (l), and (p)]. Among the four seasons, the SPEs in the middle reaches, particularly in the southern part, exhibit the closest match to the dynamic range of the reference data. This suggests that the hit bias in the middle reaches of the basin is less affected by systematic errors. In contrast, in the high-altitude areas in the upper reaches of the basin, especially during spring [see Fig. 9(a), (e), (i), and (m)], the β values are lower. This observation may be related to the snow accumulation in the Tibetan Plateau region, where IMERG is influenced by snow during the precipitation inversion process. Therefore, accurately measuring solid precipitation in complex terrain areas remains a challenge for satellite precipitation inversion. As expected, among the four SPEs, IMERG_F_Cal demonstrates the most robust performance, further validating the previous conclusion that IMERG_F_Cal is least affected by systematic errors. The supeirority of IMERG_F_Cal can be attributed to both the improvement of Final algorithm and the effect of bias-correction procedures in the process of generating IMERG_F_Cal. On the one hand, the 3.5-month time lag in the Final algorithm is primarily to incorporate more PMW estimates, which serve as a standard for calibrating IR and generating movement vectors for precipitation retrieval [48], [49], [50]. While PMW estimates for IMERG_E (delayed by about 4 h) and IMERG_L (delayed by about 12 h) are relatively rare, as these products aim to provide timely precipitation estimates. On the other hand, IMERG_F_Cal is produced by anchoring the precipitation estimates using the monthly analysis satellite–gauge product (1.0°/monthly, 1979 to the present, delayed by about 3.5 months) from the GPCC [38].

The spatial distribution of the random error σ is shown in Fig. 10. Lower values of σ indicate better performance. Overall, the winter season exhibits the lowest σ values, which can be attributed to the absence of σ values due to the presence of snow cover and reduced liquid precipitation in the upper reaches of the Yellow River Basin. While IMERG_E and IMERG_L show low σ values ($\sigma < -0.1$) in certain parts of the winter season [see Fig. 9(d) and (h)], their performance is not consistently stable and includes some significant outliers. Fortunately, the GPCC-corrected IMERG_F_Cal addresses this issue [see Fig. 10(p)]. In the summer, although IMERG_F_Cal shows relatively large random errors compared to other SPEs, with a regional average σ of 1.13 [see Fig. 10(n)], it still performs the best in terms of random error in both the spring (regional mean $\sigma = 1.0$) and autumn (regional mean $\sigma = 1.02$) seasons. IMERG_F_Cal

consistently exhibits the lowest σ values among the four SPEs [see Fig. 10(m) and (o)].

In summary, IMERG_F_Cal demonstrates the most consistent performance among the four SPEs, with the smallest random error. It performs well in terms of random error during the winter season, and despite larger random errors in the summer season, it still outperforms the other SPEs in terms of random error during the spring and autumn seasons.

IV. DISCUSSION

A. Possible Explanations for Different Error Characteristics of IMERG

In this study, a systematic evaluation of the error characteristics of three versions of four IMERG SPEs (IMERG_E, IMERG_L, IMERG_F_Uncal, and IMERG_F_Cal) at the hourly scale was conducted based on ground station observations in the Yellow River Basin of China. In addition, an improved error component method was employed to trace the sources of these errors. The results indicated that IMERG is generally able to capture the spatial distribution patterns and temporal variations of rainfall. However, it still exhibits various errors, which differ significantly across different regions, seasons, rainfall intensities, and terrain conditions. In this context, we compared our findings with previous studies to explore the potential reasons behind these errors.

First, our findings indicate that different versions of IMERG SPEs exhibit seasonal variations in performance (see Figs. 3, 6, and 7). Overall, the worst performance is observed during winter, followed by summer, while spring and autumn show better performance. This seasonal difference is most pronounced in the IMERG_F products (IMERG_F_Uncal and IMERG_F_Cal). This seasonal variation has been observed in previous studies [1], [18], [43]. The variation is mainly attributed to the differences in precipitation intensity across seasons. However, the poor performance during winter can also be attributed to factors, such as the presence of solid precipitation phases and frozen surfaces, which will be discussed in detail later. Spring, summer, and autumn are generally characterized by liquid-phase precipitation, i.e., rainfall. Our study findings reveal a significant overestimation of total precipitation by IMERG during summer in the Yellow River Basin, although this overestimation is partially offset by the positive and negative biases of missed bias and false bias (see Fig. 6). The poor performance in summer precipitation could be related to the presence of more convective rainfall during this season, and the PMW and IR sensors have limitations in accurately retrieving convective precipitation [7].

We found that in the Yellow River Basin, IMERG SPEs are significantly influenced by terrain (see Fig. 6). For example, the absolute values of total bias and hit bias for IMERG_E, IMERG_L, and IMERG_F_Uncal show a decreasing trend followed by an increasing trend as elevation increases. In aD-Dition, in spring, the absolute values of missed bias for all SPEs show an increase with higher elevation [see Fig. 6(e)–(h)]. Numerous studies have found that complex terrain can affect the precipitation monitoring capability of SPEs [22], [51], [52].

Complex terrain can influence local climate and generate orographic precipitation. Due to factors, such as beam blockage, overshooting, broadening, and ground clutter, PWM and IR sensors face challenges in capturing such precipitation events [52].

During the error characteristic analysis of IMERG SPEs, we aim to assess the monitoring capability of IMERG precipitation frequency by using the error-component method. For example, we found a significant number of false alarms in IMERG SPEs during all four seasons (see Figs. 12–15). This directly contributes to the false bias observed in IMERG SPEs throughout the seasons (see Fig. 16). In addition to inadequate monitoring of hourly precipitation events, the capability of IMERG SPEs to detect different intensity precipitation events is also limited. Based on our comparisons (see Fig. 7), we observed a clear dependence between the precipitation event detection capability of IMERG SPEs and precipitation intensity, which was also noted by Chen et al. [9]. In previous studies, the general overestimation of light precipitation and underestimation of heavy precipitation in SPEs has been a common finding [18], [34], [53]. Insufficient capture of different intensity precipitation events directly impacts the accurate estimation of precipitation amounts [54].

As mentioned earlier, IMERG SPEs perform poorly during winter, exhibiting low POD, high false alarm rate (FAR), and very high missed detection (MIS). The subpar performance of IMERG SPEs during winter can be attributed to the following factors. First, the current microwave precipitation retrieval techniques face challenges in distinguishing between the radiation signals of precipitation and strong scattering signals from land surfaces [55]. Therefore, when the winter surface consists of frozen surfaces, such as snow or ice, the PMW sensors provide limited information about effective precipitation. Second, the near-infrared sensors also have limited capability to monitor the infrared signals of winter precipitation [56]. This phenomenon has also been observed in other regions [23], [52].

During the analysis of error characteristics, we identified a notable overestimation of precipitation in the vicinity of the Yellow River channel in IMERG SPEs. Upon comparing the data, it became evident that this issue could be attributed to the presence of the river channel and small water bodies on the surface (see Fig. 11 in the Appendix). This phenomenon is likely caused by the contamination of corresponding pixels due to the presence of small water bodies or the river channel, leading to the formation of mixed pixels. The current PMW frequencies are inadequate for accurately characterizing the discrepancies in emissivity and land surface brightness temperature between water surfaces [39], [57].

B. Uncertainties

Ground-based precipitation observations are often considered to be the most reliable. However, there are still various potential errors in the error evaluation based on station observations. Firstly, station observations reflect the precipitation measurements at the specific location of the station, while the SPEs represent the estimated average precipitation at the pixel scale. Therefore, there is an issue of spatial scale mismatch [9]. As the station density becomes sparser, the error due to spatial scale mismatch increases. Thus, both station density and distribution uniformity affect the accuracy of precipitation product evaluation [58]. In fact, in high-altitude mountainous areas and regions with complex terrain, the availability of station observations is limited, and the ground-based observations may not be as "truthful" as expected. Moreover, the station observations themselves may contain errors and uncertainties.

In this study, strict screening criteria were applied to the station data used, and only SPE grids containing at least one station were considered to minimize the uncertainties introduced by station observations. However, the following uncertainties may exist: 1) the uneven distribution and limited coverage of meteorological stations may affect the evaluation results. In the Yellow River Basin, for example, the density of meteorological stations is higher in the middle and lower reaches, but lower in the upper reaches. 2) In addition, the ground-based observations reflect the precipitation at the monitoring location, while the IMERG SPEs represent the average precipitation within a spatial area of $0.1° \times 0.1°$. This spatial mismatch is a common issue in the current quantitative evaluation of SPEs, which we did not consider and can affect the evaluation results.

V. CONCLUSION

In this study, we conducted a systematic evaluation of the four IMERG SPEs from three algorithm version against ground observations over the Yellow River Basin using an improved error component decomposition method precipitation. The major conclusions can be summarized as follows.

1) IMERG SPEs have general capability in capturing precipitation patterns, but exhibit obvious spatial heterogeneity and seasonal uncertainties. IMERG_F_Cal has the highest accuracy (CC = 0.72; RMSE = 1.23 mm/d) and most stable performance with best event detection capability (POD = 52.7%; MIS = 47.3%; FAR = 59.2%). IMERG_F outperforms IMERG_E and IMERG_L. False bias is the main error component, followed by missed bias.

2) IMERG SPE errors are dependent on elevation. False bias is the main error source at elevations below 800 m in spring, summer, and autumn. While missed bias dominate the performance of IMERG SPEs due to the misdetection of precipitation events in winter.

3) IMERG SPEs' ability to capture precipitation events is strongly correlated with precipitation intensity. Except for winter, IMERG SPEs exhibit high POD and MIS values for light precipitation events. However, during winter, their performance is poor for both light precipitation and rainstorms.

4) IMERG_F_Cal has the lowest systematic and random errors, followed by IMERG_F_UnCal. IMERG_F is less affected by these errors than IMERG_E and IMERG_L. The gauge correction in IMERG_F_Cal reduces errors.

APPENDIX

TABLE II
DEFINITION OF HIT, FALSE, AND MISSED

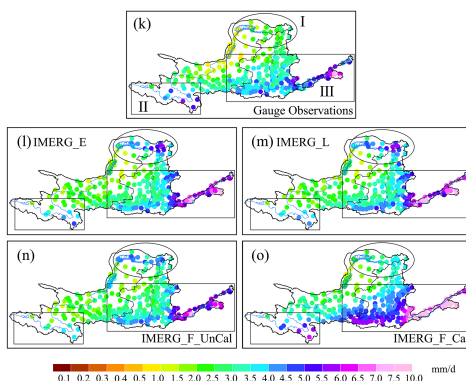|		Satellite Product	
		Rain:1	No rain:0
Gauged Observations	Rain:1	Hit	Missed
	No rain:0	False	0

Fig. 11. Spatial distribution of gauge observations (k) and four IMERG SPEs (l)–(o) summer mean daily precipitation in the Yellow River Basin, 2019–2021.
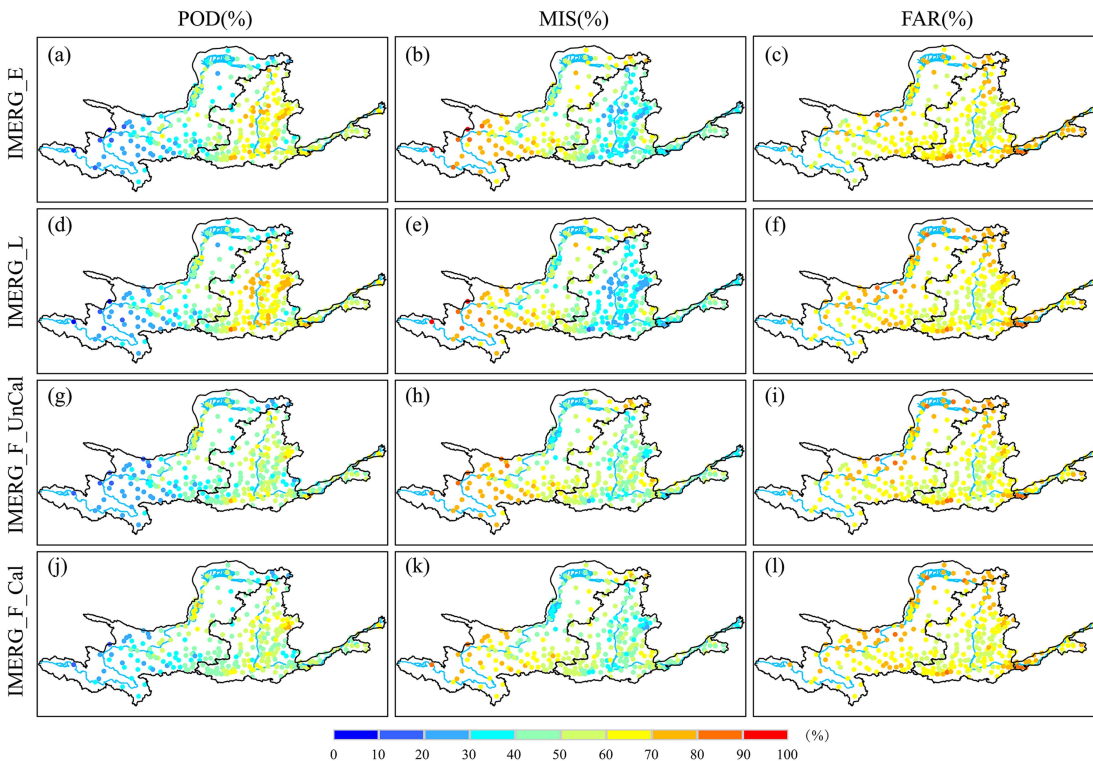

Fig. 12. IMERG SPEs spatial distribution of categorical metrics for POD, MIS and FAR in spring. IMERG_E (a)–(c); IMERG_L (d)–(f); IMERG_F_UnCal (g)–(i); IMERG_F_Cal (j)–(l), respectively. It should be noted that the 0.1mm/h rain/no rain threshold is used here.
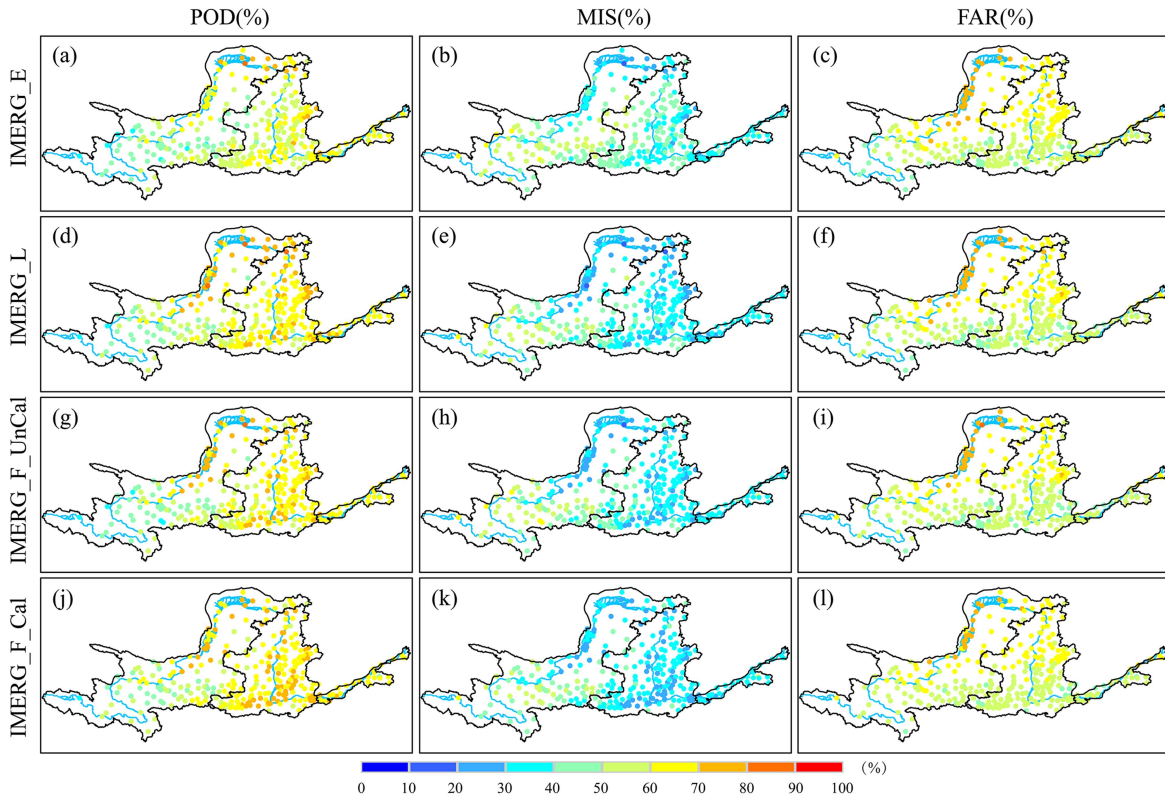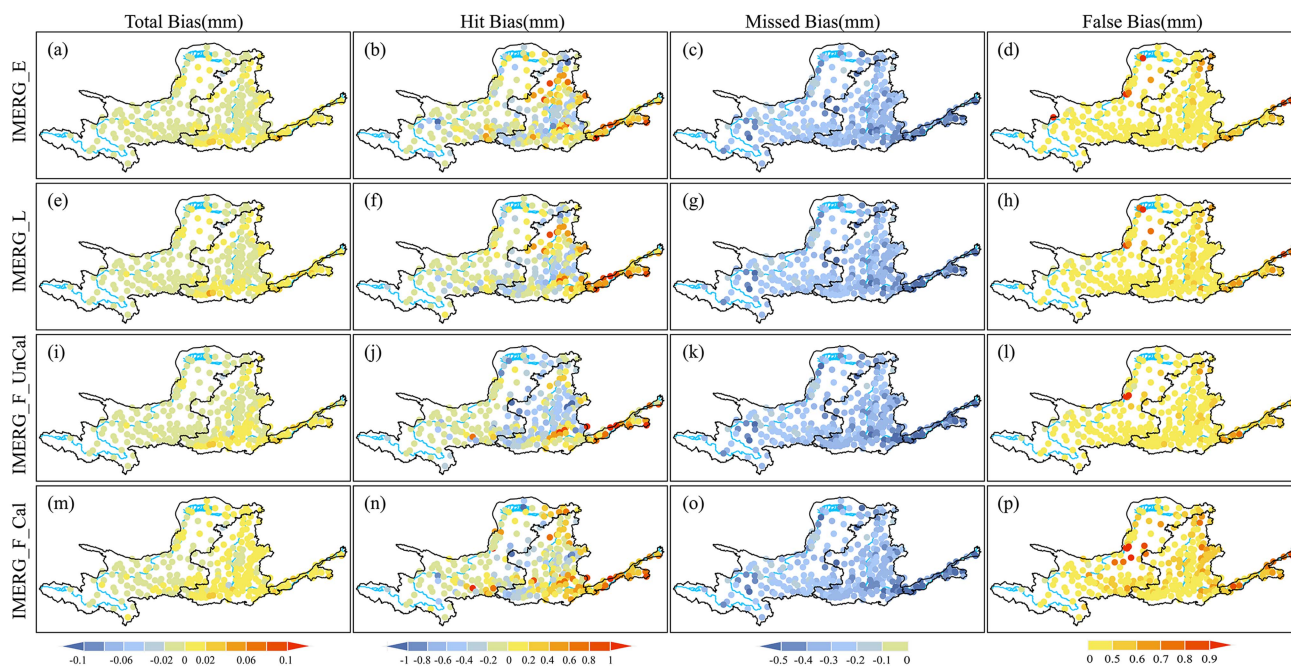
Fig. 13. IMERG SPEs spatial distribution of categorical metrics for POD, MIS and FAR in summer. IMERG_E (a)–(c); IMERG_L (d)–(f); IMERG_F_UnCal (g)–(i); IMERG_F_Cal (j)–(l), respectively. It should be noted that the 0.1 mm/h rain/no rain threshold is used here.
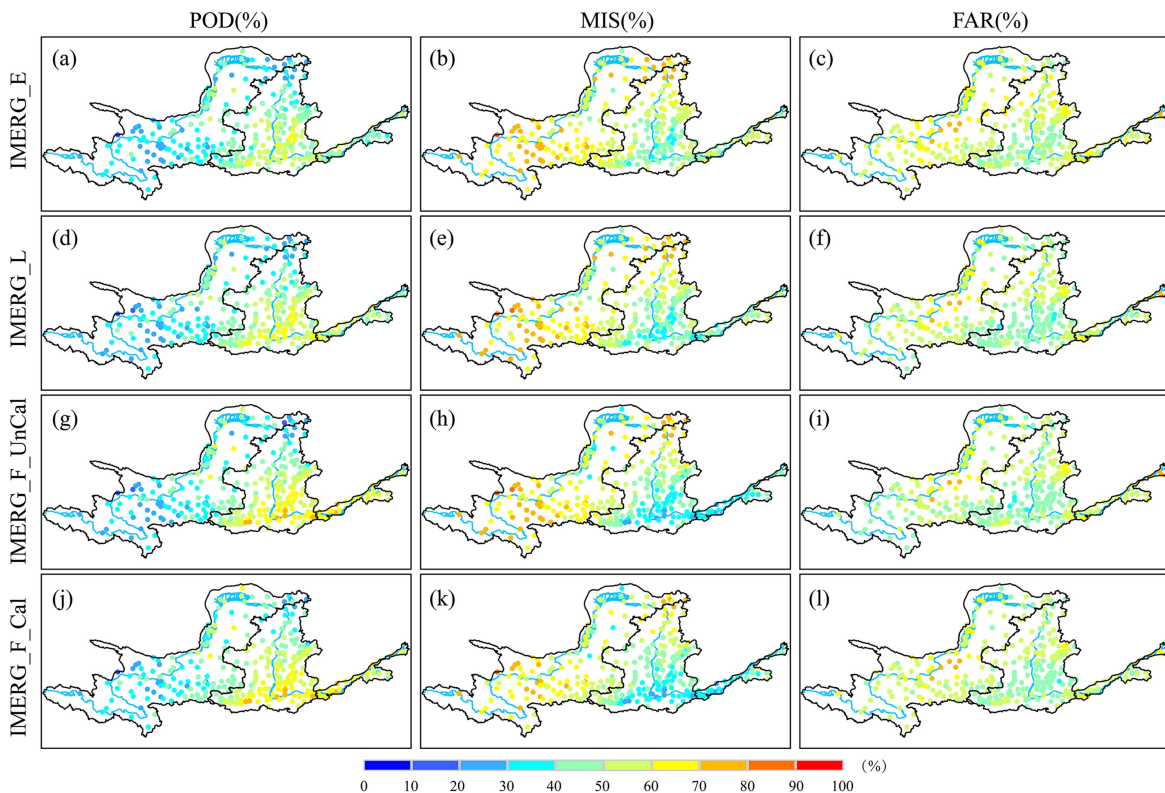
Fig. 14. IMERG SPEs spatial distribution of categorical metrics for POD, MIS and FAR in autumn. IMERG_E (a)–(c); IMERG_L (d)–(f); IMERG_F_UnCal (g)–(i); IMERG_F_Cal (j)–(l), respectively. It should be noted that the 0.1 mm/h rain/no rain threshold is used here.
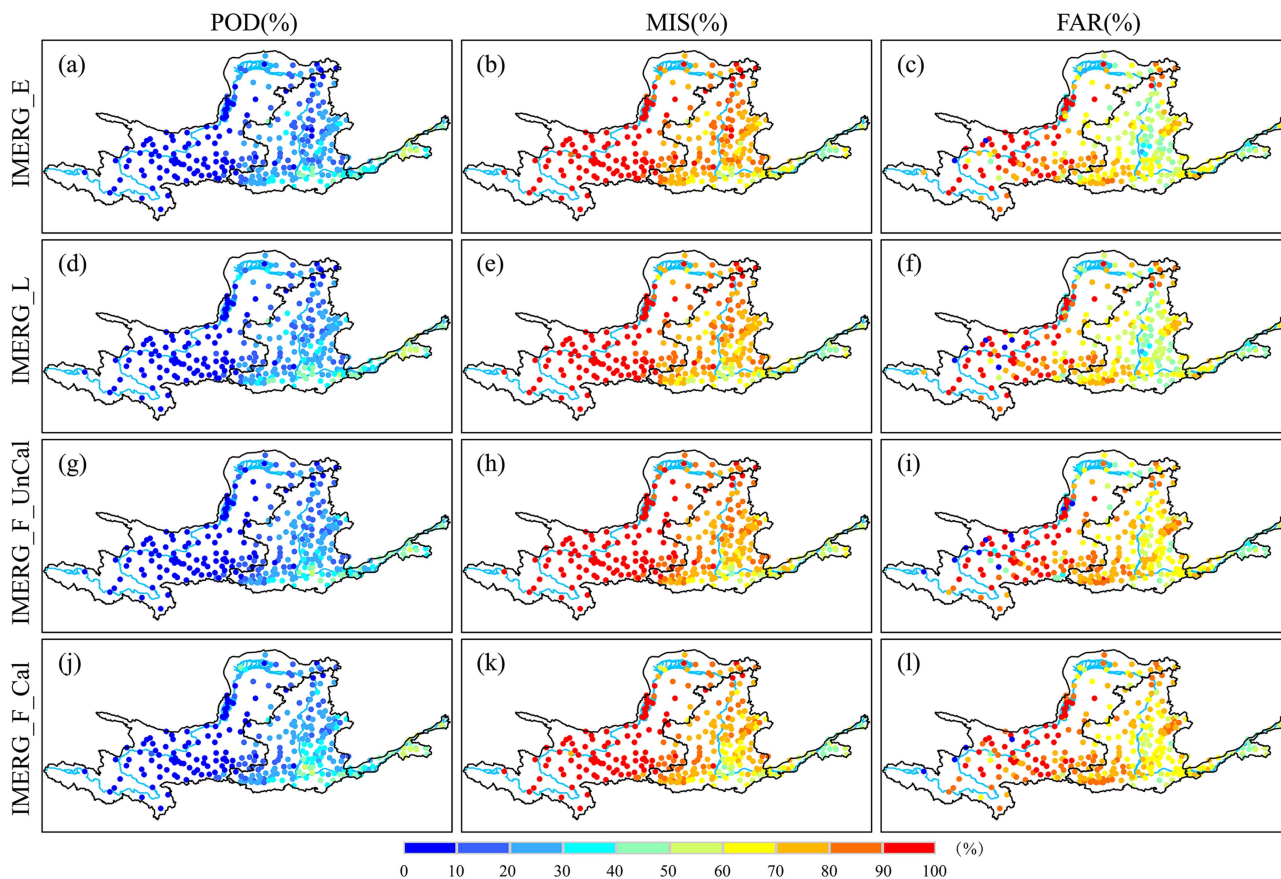
Fig. 15.   IMERG SPEs spatial distribution of categorical metrics for POD, MIS and FAR in winter. IMERG_E (a)–(c); IMERG_L (d)–(f); IMERG_F_UnCal (g)–(i); IMERG_F_Cal (j)–(l), respectively. It should be noted that the 0.1 mm/h rain/no rain threshold is used here.

Fig. 16.   Spatial distribution of the value of IMERG SPEs for total bias, hit bias, missed bias, and false bias at the hourly scale in winter. IMERG_E (a)–(d); IMERG_L (e)–(h); IMERG_F_UnCal (i)–(l); IMERG_F_Cal (m)–(p), respectively.

REFERENCES

[1] M. Y. Tang Guoqiang, L. Di, Z. Lingzhi, and H. Yang, "Evaluation of GPM day-1 IMERG and TMPA version-7 legacy products over mainland China at multiple spatiotemporal scales," *J. Hydrol.*, vol. 533, pp. 152–167, 2016, doi: 10.1016/j.jhydrol.2015.12.008.

[2] G. Skofronick-Jackson et al., "The global precipitation measurement (GPM) mission for science and society," *Bull. Amer. Meteorological Soc.*, vol. 98, no. 8, pp. 1679–1695, 2017, doi: 10.1175/bams-d-15-00306.1.

[3] J. Su, X. Li, W. Ren, H. Lü, and D. Zheng, "How reliable are the satellite-based precipitation estimations in guiding hydrological modelling in South China?," *J. Hydrol.*, vol. 602, 2021, Art. no. 126705, doi: 10.1016/j.jhydrol.2021.126705.

[4] G. J. Huffman, "Global precipitation at one-degree daily resolution from multisatellite observations," *J. Hydrol.*, vol. 2, pp. 36–50, 2000.

[5] H. Wang, Y. Yuan, S. Zeng, W. Li, and X. Tang, "Evaluation of satellite-based precipitation products from GPM IMERG and GSMaP over the three-river headwaters region, China," *Hydrol. Res.*, vol. 52, no. 6, pp. 1328–1343, 2021, doi: 10.2166/nh.2021.029.

[6] W. Qi, B. Yong, and J. J. Gourley, "Monitoring the super typhoon Lekima by GPM-based near-real-time satellite precipitation estimates," *J. Hydrol.*, vol. 603, 2021, Art. no. 126968, doi: 10.1016/j.jhydrol.2021.126968.

[7] Z. Bi et al., "Systematic assessment of GPM IMERG V06 precipitation products with dense rain gauge observations over Zhejiang province, China," *Int. J. Climatol.*, vol. 42, no. 16, pp. 9471–9493, 2022, doi: 10.1002/joc.7838.

[8] L. da Silva, M. Mahmoud, L. González-Rodríguez, S. Mohammed, L. Rodríguez-López, and M. Arias, "Assessment of the IMERG early-run precipitation estimates over South American country of Chile," *Remote Sens.*, vol. 15, no. 3, 2023, Art. no. 573, doi: 10.3390/rs15030573.

[9] H. Chen, B. Yong, Y. Shen, J. Liu, Y. Hong, and J. Zhang, "Comparison analysis of six purely satellite-derived global precipitation estimates," *J. Hydrol.*, vol. 581, 2020, Art. no. 124376, doi: 10.1016/j.jhydrol.2019.124376.

[10] S. Jiang et al., "Statistical and hydrological evaluation of the latest integrated multi-satellite Retrievals for GPM (IMERG) over a midlatitude humid basin in South China," *Atmospheric Res.*, vol. 214, pp. 418–429, 2018, doi: 10.1016/j.atmosres.2018.08.021.

[11] Z. Wang, R. Zhong, C. Lai, and J. Chen, "Evaluation of the GPM IMERG satellite-based precipitation products and the hydrological utility," *Atmospheric Res.*, vol. 196, pp. 151–163, 2017, doi: 10.1016/j.atmosres.2017.06.020.

[12] P. Li et al., "Assessment on IMERG V06 precipitation products using rain gauge data in Jinan city, Shandong province, China," *Remote Sens.*, vol. 13, no. 7, 2021, Art. no. 1241, doi: 10.3390/rs13071241.

[13] N. Bulovic, N. McIntyre, and F. Johnson, "Evaluation of IMERG V05B 30-min rainfall estimates over the high-elevation tropical andes mountains," *J. Hydrometeorol.*, vol. 21, no. 12, pp. 2875–2892, 2020, doi: 10.1175/jhm-d-20-0114.1.

[14] J. P. Kiyoung Kim, J. Baik, and M. Choi, "Evaluation of topographical and seasonal feature using GPM IMERG and TRMM 3B42 over far-east Asia," *Atmospheric Res.*, vol. 187, pp. 95–105, 2017.

[15] C. Meng, X. Mo, S. Liu, and S. Hu, "Extensive evaluation of IMERG precipitation for both liquid and solid in yellow river source region," *Atmospheric Res.*, vol. 256, 2021, Art. no. 105570, doi: 10.1016/j.atmosres.2021.105570.

[16] H. Chen, B. Yong, W. Qi, H. Wu, L. Ren, and Y. Hong, "Investigating the evaluation uncertainty for satellite precipitation estimates based on two different ground precipitation observation products," *J. Hydrometeorol.*, vol. 21, no. 11, pp. 2595–2606, 2020, doi: 10.1175/jhm-d-20-0103.1.

[17] H. Chen et al., "Impact of the crucial geographic and climatic factors on the input source errors of GPM-based global satellite precipitation estimates," *J. Hydrol.*, vol. 575, pp. 1–16, 2019, doi: 10.1016/j.jhydrol.2019.05.020.

[18] S. Moazami and M. R. Najafi, "A comprehensive evaluation of GPM-IMERG V06 and MRMS with hourly ground-based precipitation observations across Canada," *J. Hydrol.*, vol. 594, 2021, Art. no. 125929, doi: 10.1016/j.jhydrol.2020.125929.

[19] R. Li, C. Guilloteau, P. - E. Kirstetter, and E. Foufoula-Georgiou, "How well does the IMERG satellite precipitation product capture the timing of precipitation events?," *J. Hydrol.*, vol. 620, 2023, Art. no. 129563, doi: 10.1016/j.jhydrol.2023.129563.

[20] Y. Tian, G. S. Nearing, C. D. Peters-Lidard, K. W. Harrison, and L. Tang, "Performance metrics, error modeling, and uncertainty quantification," *Monthly Weather Rev.*, vol. 144, no. 2, pp. 607–613, 2016, doi: 10.1175/mwr-d-15-0087.1.

[21] Y. Tian et al., "Component analysis of errors in satellite-based precipitation estimates," *J. Geophysical Res.*, vol. 114, no. D24, pp. 3087–3104, 2009, doi: 10.1029/2009jd011949.

[22] B. Yong, B. Chen, Y. Tian, Z. Yu, and Y. Hong, "Error-component analysis of TRMM-based multi-satellite precipitation estimates over mainland China," *Remote Sens.*, vol. 8, no. 5, 2016, Art. no. 440, doi: 10.3390/rs8050440.

[23] H. Guo, A. Bao, F. Ndayisaba, T. Liu, A. Kurban, and P. De Maeyer, "Systematical evaluation of satellite precipitation estimates over central Asia using an improved error-component procedure," *J. Geophysical Res.: Atmospheres*, vol. 122, no. 20, pp. 10906–10927, 2017, doi: 10.1002/2017jd026877.

[24] L. Tang, Y. Tian, F. Yan, and E. Habib, "An improved procedure for the validation of satellite-based precipitation estimates," *Atmospheric Res.*, vol. 163, pp. 61–73, 2015, doi: 10.1016/j.atmosres.2014.12.016.

[25] G. Tang, M. P. Clark, S. M. Papalexiou, Z. Ma, and Y. Hong, "Have satellite precipitation products improved over last two decades? A comprehensive comparison of GPM IMERG with nine satellite and reanalysis datasets," *Remote Sens. Environ.*, vol. 240, 2020, Art. no. 111697, doi: 10.1016/j.rse.2020.111697.

[26] X. Li, O. Sang, N. Wang, L. Liu, and Y. Huang, "Evaluation of the GPM IMERG V06 products for light rain over Mainland China," *Atmospheric Res.*, vol. 253, 2021, Art. no. 245620, doi: 10.1016/j.atmosres.2021.105510.

[27] H. Wu, B. Yong, Z. Shen, and W. Qi, "Comprehensive error analysis of satellite precipitation estimates based on Fengyun-2 and GPM over Chinese mainland," *Atmospheric Res.*, vol. 263, 2021, Art. no. 105805, doi: 10.1016/j.atmosres.2021.105805.

[28] Y. Wang, C. Miao, X. Zhao, Q. Zhang, and J. Su, "Evaluation of the GPM IMERG product at the hourly timescale over China," *Atmospheric Res.*, vol. 285, 2023, Art. no. 106656, doi: 10.1016/j.atmosres.2023.106656.

[29] R. Li, K. Wang, and D. Qi, "Event-based evaluation of the GPM multisatellite merged precipitation product from 2014 to 2018 over China: Methods and results," *J. Geophysical Res.: Atmospheres*, vol. 126, no. 1, 2021, Art. no. e2020JD033692, doi: 10.1029/2020jd033692.

[30] J. Meng, L. Li, Z. Hao, J. Wang, and Q. Shao, "Suitability of TRMM satellite rainfall in driving a distributed hydrological model in the source region of Yellow River," *J. Hydrol.*, vol. 509, pp. 320–332, 2014, doi: 10.1016/j.jhydrol.2013.11.049.

[31] J. Su, H. Lü, J. Wang, A. Sadeghi, and Y. Zhu, "Evaluating the applicability of four latest satellite–gauge combined precipitation estimates for extreme precipitation and streamflow predictions over the upper yellow river basins in China," *Remote Sens.*, vol. 9, no. 11, 2017, Art. no. 1176, doi: 10.3390/rs9111176.

[32] Y. Shen and A. Xiong, "Validation and comparison of a new gauge-based precipitation analysis over mainland China," *Int. J. Climatol.*, vol. 36, no. 1, pp. 252–265, 2016, doi: 10.1002/joc.4341.

[33] Y. Shen, A. Xiong, Y. Wang, and P. Xie, "Performance of high-resolution satellite precipitation products over China," *J. Geophysical Res.*, vol. 115, no. D2, 2010, Art. no. 6277, doi: 10.1029/2009jd012097.

[34] H. Guo et al., "Early assessment of integrated multi-satellite retrievals for global precipitation measurement over China," *Atmospheric Res.*, vol. 176-177, pp. 121–133, 2016, doi: 10.1016/j.atmosres.2016.02.020.

[35] H. Guo et al., "Assessment of three long-term satellite-based precipitation estimates against ground observations for drought characterization in northwestern China," *Remote Sens.*, vol. 14, no. 4, 2022, Art. no. 828, doi: 10.3390/rs14040828.

[36] M. Gosset, J. Viarre, G. Quantin, and M. Alcoba, "Evaluation of several rainfall products used for hydrological applications over West Africa using two high-resolution gauge networks," *Quart. J. Roy. Meteorological Soc.*, vol. 139, no. 673, pp. 923–940, 2013, doi: 10.1002/qj.2130.

[37] Y. Tian, C. D. Peters-Lidard, B. J. Choudhury, and M. Garcia, "Multitemporal analysis of TRMM-based satellite precipitation products for land data assimilation applications," *J. Hydrometeorol.*, vol. 8, no. 6, pp. 1165–1183, 2007, doi: 10.1175/2007jhm859.1.

[38] Z. Ma et al., "AIMERG: A new Asian precipitation dataset (0.1°/half-hourly, 2000–2015) by calibrating the GPM-era IMERG at a daily scale using APHRODITE," *Earth System Sci. Data*, vol. 12, no. 3, pp. 1525–1544, 2020, doi: 10.5194/essd-12-1525-2020.

[39] J. Ringard, M. Becker, F. Seyler, and L. Linguet, "Temporal and spatial assessment of four satellite rainfall estimates over French Guiana and North Brazil," *Remote Sens.*, vol. 7, no. 12, pp. 16441–16459, 2015, doi: 10.3390/rs71215831.

[40] T. Dinku, P. Ceccato, E. Grover-Kopec, M. Lemma, S. J. Connor, and C. F. Ropelewski, "Validation of satellite rainfall products over East Africa's complex topography," *Int. J. Remote Sens.*, vol. 28, no. 7, pp. 1503–1526, 2007, doi: 10.1080/01431160600954688.

[41] X. Tang, H. Li, G. Qin, Y. Huang, and Y. Qi, "Evaluation of satellite-based precipitation products over complex topography in mountainous Southwestern China," *Remote Sens.*, vol. 15, no. 2, 2023, Art. no. 473, doi: 10.3390/rs15020473.

[42] Y. Ma et al., "Similarity and error intercomparison of the GPM and its predecessor-TRMM multisatellite precipitation analysis using the best available hourly gauge network over the Tibetan plateau," *Remote Sens.*, vol. 8, no. 7, 2016, Art. no. 569, doi: 10.3390/rs8070569.

[43] X. Wu, J. Su, W. Ren, H. Lü, and F. Yuan, "Statistical comparison and hydrological utility evaluation of ERA5-Land and IMERG precipitation products on the Tibetan plateau," *J. Hydrol.*, vol. 620, 2023, Art. no. 129384, doi: 10.1016/j.jhydrol.2023.129384.

[44] D. Lu and B. Yong, "A preliminary assessment of the gauge-adjusted near-real-time GSMaP precipitation estimate over mainland China," *Remote Sens.*, vol. 12, no. 1, 2020, Art. no. 141, doi: 10.3390/rs12010141.

[45] H. Chen, B. Yong, P. - E. Kirstetter, L. Wang, and Y. Hong, "Global component analysis of errors in three satellite-only global precipitation estimates," *Hydrol. Earth System Sci.*, vol. 25, no. 6, pp. 3087–3104, 2021, doi: 10.5194/hess-25-3087-2021.

[46] Y. Hong, D. Gochis, J.-T. Cheng, K.-L. Hsu, and S. Sorooshian, "Evaluation of PERSIANN-CCS rainfall measurement using the NAME event rain gauge network," *J. Hydrometeorol.*, vol. 8, no. 3, pp. 469–482, 2007, doi: 10.1175/jhm574.1.

[47] F. Gan et al., "Performance evaluation of IMERG products based on the extremely heavy rainstorm event (2021) once in a thousand years in Henan, China," *Atmospheric Res.*, vol. 285, 2023, Art. no. 106639, doi: 10.1016/j.atmosres.2023.106639.

[48] J. Tan, W. A. Petersen, and A. Tokay, "A novel approach to identify sources of errors in IMERG for GPM ground validation," *J. Hydrometeorol.*, vol. 17, no. 9, pp. 2477–2491, 2016, doi: 10.1175/jhm-d-16-0079.1.

[49] J. M. D. S. Afonso et al., "Precipitation diurnal cycle assessment of satellite-based estimates over Brazil," *Remote Sens.*, vol. 12, no. 14, 2020, Art. no. 2339, doi: 10.3390/rs12142339.

[50] O. S., U. Foelsche, G. Kirchengast, J. Fuchsberger, J. Tan, and W. A. Petersen, "Evaluation of GPM IMERG early, late, and final rainfall estimates using WegenerNet gauge data in Southeastern Austria," *Hydrol. Earth System Sci.*, vol. 21, no. 12, pp. 6559–6572, 2017, doi: 10.5194/hess-21-6559-2017.

[51] J. Su, H. Lü, Y. Zhu, X. Wang, and G. Wei, "Component analysis of errors in four GPM-based precipitation estimations over mainland China," *Remote Sens.*, vol. 10, no. 9, 2018, Art. no. 1420, doi: 10.3390/rs10091420.

[52] S. Chen et al., "Intercomparison of precipitation estimates from WSR-88D radar and TRMM measurement over continental United States," *IEEE Trans. Geosci. Remote Sens.*, vol. 53, no. 8, pp. 4444–4456, Aug. 2015, doi: 10.1109/tgrs.2015.2399307.

[53] P. Weng, Y. Tian, Y. Jiang, D. Chen, and J. Kang, "Assessment of GPM IMERG and GSMaP daily precipitation products and their utility in droughts and floods monitoring across Xijiang River Basin," *Atmospheric Res.*, vol. 286, 2023, Art. no. 106673, doi: 10.1016/j.atmosres.2023.106673.

[54] M. Tan, A. Ibrahim, Z. Duan, A. Cracknell, and V. Chaplot, "Evaluation of six high-resolution satellite and ground-based precipitation products over Malaysia," *Remote Sens.*, vol. 7, no. 2, pp. 1504–1528, 2015, doi: 10.3390/rs70201504.

[55] A. Behrangi et al., "Satellite-based precipitation estimation and its application for streamflow prediction over mountainous western U.S. Basins," *J. Appl. Meteorol. Climatol.*, vol. 53, no. 12, pp. 2823–2842, 2014, doi: 10.1175/jamc-d-14-0056.1.

[56] B. Yong, "Comments on 'error analysis of satellite precipitation products in mountainous basins'," *J. Hydrometeorol.*, vol. 16, no. 3, pp. 1443–1444, 2015, doi: 10.1175/jhm-d-14-0202.1.

[57] M. O. Karaseva, S. Prakash, and R. M. Gairola, "Validation of high-resolution TRMM-3B43 precipitation product using rain gauge measurements over Kyrgyzstan," *Theor. Appl. Climatol.*, vol. 108, no. 1-2, pp. 147–157, 2011, doi: 10.1007/s00704-011-0509-6.

[58] C. Miao, H. Ashouri, K. - L. Hsu, S. Sorooshian, and Q. Duan, "Evaluation of the PERSIANN-CDR daily rainfall estimates in capturing the behavior of extreme precipitation events over China," *J. Hydrometeorol.*, vol. 16, no. 3, pp. 1387–1396, 2015, doi: 10.1175/jhm-d-14-0174.1.

Yunfei Tian (Student Member, IEEE) is currently working toward the master's degree in cartography and geographic information systems with the School of Geography and Tourism, Qufu Normal University, Rizhao, China.

Her research interests include quantitative estimation of satellite-based precipitation products and the monitoring of extreme precipitation events.

Xiaoyu Lv is currently working toward the master's degree in cartography and geographic information systems with the School of Geography and Tourism, Qufu Normal University, Rizhao, China.

She has authored/coauthored six articles. Her research interests include drought monitoring and remote sensing precipitation evaluation.

Hao Guo received the Ph.D. degree in cartography and geographic information systems from both Ghent University, Ghent, Belgium, and the University of Chinese Academy of Sciences, Beijing, China, in 2019.

He is currently a Vice Professor with the School of Geography and Tourism, Qufu Normal University, Rizhao, China. He authored or coauthored more than 40 SCI-indexed peer-reviewed papers. His primary research interests include the estimation of land surface variables from satellite observations and the monitoring of extreme weather-climate events.

Junli Li received the Ph.D. degree in photogrammetry and remote sensing from the School of Remote Sensing, Wuhan University, Wuhan, China, in 2007.

Since 2007, he has been working with the Xinjiang Institute of Ecology and Geography, Chinese Academy of Sciences, Beijing, China. From 2008 to 2010, he conducted postdoctoral research with the Department of Geography, University of California, Los Angeles, CA, USA. He has authored or coauthored more than 60 papers covering topics, such as remote sensing information extraction, lake changes, and mechanisms of water resource changes in arid regions. His research interests include applied remote sensing, including thematic information extraction, water resource changes in arid regions, and spatiotemporal patterns of lakes in Central Asia.

Xiangchen Meng (Member, IEEE) received the M.Sc. degree in photogrammetry and remote sensing from the Shandong University of Science and Technology, Qingdao, China, in 2016, and the Ph.D. degree in cartography and geographic information system from Beijing Normal University, Beijing, China, in 2020.

He is currently a Lecturer at the School of Geography and Tourism, Qufu Normal University, Rizhao, China. His research interests include the retrieval and validation of land surface temperature/emissivity from satellite data.

Li Zhu received the master's degree in ecology from the University of Chinese Academy of Sciences, Beijing, China, in 2016.

She is currently a Librarian with the School of Geography and Tourism, Qufu Normal University, Rizhao, China. Her research interests include drought monitoring and risk assessment.

Chunrui Guo is currently working toward the master's degree in cartography and geographic information systems with the School of Geography and Tourism, Qufu Normal University, Rizhao, China.

Her research interests include detection and risk assessment of extreme precipitation events.

Philippe De Maeyer (Member, IEEE) received the Ph.D. degree in sciences from Université Bordeaux I, Talence, France, in 1980.

He is a Senior Full Professor in cartography and GIS with Ghent University, Ghent, Belgium. His research interests include applied GIS, esp.: use of GIS and remote sensing in archaeology, risk and land-use issues including risks of climate change (esp. Central-Asia), use of GIS for risk modeling of floods and other natural hazards, use of GIS for accessibility to health care, etc.